

OPTICAL-NEAR INFRARED COLOR GRADIENTS AND MERGING HISTORY OF ELLIPTICAL GALAXIES

Duho Kim^{1,2} & Myungshin Im¹

Draft version August 21, 2018

ABSTRACT

It has been suggested that merging plays an important role in the formation and the evolution of elliptical galaxies. While gas dissipation by star formation is believed to steepen metallicity and color gradients of the merger products, mixing of stars through dissipation-less merging (dry merging) is believed to flatten them. In order to understand the past merging history of elliptical galaxies, we studied the optical-near infrared (NIR) color gradients of 204 elliptical galaxies. These galaxies are selected from the overlap region of the Sloan Digital Sky Survey (SDSS) Stripe 82 and the UKIRT Infrared Deep Sky Survey (UKIDSS) Large Area Survey (LAS). The use of the optical and the NIR data (g , r , and K) provides large wavelength baselines, and breaks the age-metallicity degeneracy, allowing us to derive age and metallicity gradients. The use of the deep SDSS Stripe 82 images make it possible for us to examine how the color/age/metallicity gradients are related to merging features. We find that the optical-NIR color and the age/metallicity gradients of elliptical galaxies with tidal features are consistent with those of relaxed ellipticals suggesting that the two populations underwent a similar merging history on average and that mixing of stars was more or less completed before the tidal features disappear. Elliptical galaxies with dust features have steeper color gradients than the other two types, even after masking out dust features during the analysis, which can be due to a process involving wet merging. More importantly, we find that the scatter in the color/age/metallicity gradients of the relaxed and merging feature types, decreases as their luminosities (or masses) increase at $M > 10^{11.4} M_{\odot}$ but stays to be large at lower luminosities. Mean metallicity gradients appear nearly constant over the explored mass range, but a possible flattening is observed at the massive end. According to our toy model that predicts how the distribution of metallicity gradients changes as a result of major dry merging, the mean metallicity gradient should flatten by 40% and its scatter become smaller by 80% per a mass doubling scale if ellipticals evolve only through major dry merger. Our result, although limited by a number statistics at the massive end, is consistent with the picture that major dry merging is an important mechanism for the evolution for ellipticals at $M > 10^{11.4} M_{\odot}$, but less important at the lower mass range.

Subject headings: galaxies: elliptical and lenticular, cD — galaxies: evolution — galaxies: interactions — galaxies: peculiar

1. INTRODUCTION

Elliptical galaxies are featureless, elliptical stellar systems, predominantly made with old stars. They are a prime object in the currently popular hierarchical galaxy formation models under the Λ CDM universe, since in a cold-dark matter dominated universe, galaxies grow through merging with other galaxies, and it is well-known from simulations that merging between galaxies with comparable masses (called major merger) produce galaxies with the characteristics of ellipticals (Toomre 1977; Barnes & Hernquist 1992; Naab & Trujillo 2006). Therefore, studying elliptical galaxies is important to test our current theoretical understanding of the galaxy formation and the evolution mechanism.

Many observational works have been performed for elliptical galaxies near and far, but our understanding on the evolution of elliptical galaxies is still far from complete. On one hand, there are pieces of observational evidence for a complex history in the evolu-

tion of elliptical galaxies in support of the hierarchical merging picture. For example, very deep imaging data reveal more than 70% of elliptical galaxies with tidally disrupted features that are indicative of their past merging history (e.g., Tal et al. 2009; van Dokkum 2005; Sheen et al. 2012). Small levels of recent star formation are found as blue cores in some ellipticals (e.g., Im et al. 2001; Lee et al. 2006) and the UV excess light (Yi et al. 2005) or as excessive MIR fluxes (Ko et al. 2009, 2012; Shim et al. 2011; Hwang et al. 2012). These results break a simplistic view of the monolithic collapse model (Eggen et al. 1962; Larson 1974) that ellipticals are old galaxies with little merging nor recent star formation activities. While these observational evidence point toward the hierarchical build-up of elliptical galaxies, other properties of ellipticals do not bode well with the merger scenario. Tight scaling correlations relations are observed for early-type galaxies, such as the fundamental plane relation (e.g., Djorgovski & Davis 1987; Jun & Im 2008), and the color-magnitude relation (Baum 1959; Visvanathan & Sandage 1977). Also, the number density of early-type galaxies does not evolve as drastically as some of the simple hierarchical merging models have predicted (Im et al. 1999, 2002; Scarlata et al. 2007).

The observational results that appear contradictory to

¹Center for the Exploration of the Origin of the Universe (CEO), Astronomy Program, Department of Physics and Astronomy, Seoul National University, 1 Gwanak-rho, Gwanak-gu, Seoul 151-742, South Korea

²School of Earth and Space Exploration, Arizona State University, P.O. Box 871404, Tempe, AZ 85287-1404, USA

each other can be reconciled by introducing dry merging in the evolution of elliptical galaxies. Dry (or dissipationless) merging is a process where two gas-poor galaxies with old stellar population merge together to create a more massive, old galaxy. Although a dissipative merging between gas-rich galaxies (wet merging) inevitably introduces scatters in various scaling relations and too many blue ellipticals, the dry merging offers a way to avoid such a situation while allowing frequent merging activities in the hierarchical merging models. This is possible since dry merging preserves the red colors of the already old pre-mergers, avoiding the introduction of additional scatters in the scaling relations arising from new star formation as is the case for wet merging. Dry merging is also gaining popularity as a possible mechanism to explain the observed rapid growth in sizes of early-type galaxies from high to low redshifts (van Dokkum et al. 2008; Trujillo et al. 2006; Daddi et al. 2005)

One of interesting consequences of dry merging can be found in the radial gradient of various properties, such as the metallicity, the age, and the colors of ellipticals. It has been known that centers of low redshift elliptical galaxies are redder than their outskirts (e.g. Franx & Illingworth 1990; Peletier et al. 1990; Tamura & Ohta 2003), and this radial change of color is called the color gradient. The color gradient is in general attributed to a gradient in metallicity although a small amount of the age gradient is known to contribute to the color gradient, where low redshift ellipticals show the higher metallicities and the younger stellar ages at the center than in the outskirt. According to line indices analysis studies, the metallicity gradients have a mean value of about -0.2 to -0.3 per a decade change in radius while the slope of the age gradient is known to be of order of -0.1 or less (Ogando et al. 2005; Spolaor et al. 2010; Kuntschner et al. 2010). The metallicity and the age gradients can be derived from color profiles and such studies tend to implicate the metallicity gradients of order of -0.4 (La Barbera et al. 2010; Tortora & Napolitano 2012), steeper than the spectroscopically determined metallicity gradients. The origin of the discrepancy between the spectroscopic and the photometric studies is not clear, but could be related to a difference in the explored range of radius. In the spectroscopic studies, the gradients are determined within r_{eff} (effective radius), while the photometric studies extend the radius coverage to a few $\times r_{eff}$.

When a monolithic collapse of the proto-galactic gas creates an elliptical galaxy, star formation can occur over several generations at center using the gas that is retained by a strong gravitational potential in the central part of the galaxy. The gas is enriched by previous episodes of star formation, so stars in the central part are expected to have a high metallicity. On the other hand, the star formation truncates earlier in the outer region of an elliptical galaxy since the gas is lost easily due to a shallow gravitational potential preventing further episodes of star formation. The net result is that an elliptical would have stars with higher metallicity and a bit younger mean stellar age at the inner region than the outer region, creating the metallicity, the age, and the color gradients that are in qualitative agreement with the observed results. A similar situation is expected to occur after mergers of two gas-rich galaxies. However,

according to the formation models of ellipticals through monolithic collapses of proto-galactic gas, the metallicity gradient is predicted to be quite steep, with 0.5 to 1 in the logarithmic value of metallicity per one dex change in radius (Larson 1974; Carlberg 1984; Kawata & Gibson 2003). Simulations that implement merging activities predict that the metallicity gradient is shallower at -0.2 – -0.3 (e.g., Kobayashi 2004; Hopkins et al. 2009).

Dry merging modifies the above theoretical picture in the following way. When two gas-poor galaxies with a comparable mass merge (“major dry merging”), a re-distribution of stars dilute the metallicity gradient, therefore flattening it in the post-merger (e.g. White 1980; Ko & Im 2005; Di Matteo et al. 2009). An opposite trend is suggested to occur during minor dry merging, i.e., merging between ellipticals with very different masses (mass ratios of 5–10 to 1 or larger), where stars in a minor companion galaxy get deposited at a large distance from the center of the main pre-merging galaxy, avoiding stars to be mixed throughout the main galaxy, contrary to the case of major dry merging (Bernardi et al. 2011). Observations offer somewhat mixed views about the importance of dry merging, and the results from some of such studies are presented below. Roche et al. (2010) find that color gradients of the brightest cluster galaxies (BCGs) are flatter than those of non-BCGs. They conclude that a great number of dry merging events flattened C-M relation and individual BCG. Ko & Im (2005) find color-gradients are flatter for elliptical galaxies in the cluster environment than in field, suggesting more frequent merging history in the high density environment. Spolaor et al. (2010) derived the metallicity gradients of 51 nearby early-type galaxies using their spectroscopic data and find a flattening trend in the metallicity gradients toward a large galaxy mass but with a large scatter. Their interpretation of the result is that galaxies with a few $\times 10^{10} M_{\odot}$ are created through wet merging, but evolved via dry merging thereafter. The increase in the scatter of the metallicity gradient is also found in other studies (e.g., Ogando et al. 2005), and some works interpret that the increase in the scatter is suggested is caused by dry merging of objects with a variety of metallicity gradients (e.g., Di Matteo et al. 2009). However, such an interpretation requires galaxies with steep gradients to create merger products with a large scatter, and the number of such galaxies with steep gradients should decrease as galaxies experience successive dry merging events. This will inevitably reduce the scatter in the mass-metallicity gradient relation at high mass end, which is inconsistent with the observed trend. Also, Pipino et al. (2010) show that the large dispersion can be explained under the frame work of the monolithic collapse models where various star formation efficiencies produce the difference in gradients with the most efficient star formation creating the steepest gradient.

In this paper, we will examine the color/age/metallicity gradients and their connection to dry merging, analyzing the optical and the NIR imaging data of a sample of 204 nearby elliptical galaxies that are divided into three different types – ones showing no merging feature, ones with tidal-feature (as a result of merging), and ones with dust-feature. We will also present a simple model that predicts the evolution of the mass-metallicity gradient relation under

major dry merging. This model will be used to interpret our result.

The use of the optical and the NIR data allows us to break the age-metallicity degeneracy that usually hampers the interpretation of colors of early-type galaxies with optical data alone (Worthey 1994; Saglia et al. 2000; Bell & de Jong 2000; Li et al. 2007). The large wavelength baseline between the optical and the NIR are also advantageous in deriving color gradients which are known to be shallow in optical bands (Hinkley & Im 2001; La Barbera et al. 2010). Also, NIR data, especially K -band, of an elliptical galaxy is known to be a good indicator of stellar mass, since mass-to-light ratios (M/L) in NIR are less sensitive to galaxy types or ages than in the optical (Bell & de Jong 2001; Pahre et al. 1995; Jun & Im 2008). Here, we will use the K -band light as a mass indicator of elliptical galaxies.

Our sample will be drawn from a sample of early-type galaxies in Kaviraj (2010) which classifies early type galaxies based on merging features. They are galaxies with very deep imaging data reaching down to the surface brightness (SB) limit of $\mu_r \sim 26$ mag arcsec $^{-2}$, enabling us to subdivide and examine elliptical galaxies into three different types that reflect different stages of merging. The relaxed types are objects without strong merging feature. If they had undergone merging in the past, and they should have done so a long time ago ($>$ several Gyrs). Presumably, such objects should have well-established gradient properties with tighter scatters. The tidal feature types are objects that underwent merging relatively recently ($<$ several Gyrs). They may or may not share the gradient properties similar to the relaxed types, but we can expect the gradient properties to be less established than the relaxed-types with a somewhat larger scatter. Finally, the dust-feature types are objects with dust and gas, and they are suggested to be involved in a merger with a gas-rich companion (e.g. Kaviraj et al. 2012). Therefore, such objects need to be considered separately when examining dry merging.

Throughout this paper, we adopt a concordance cosmology of $\Omega_m = 0.3$, $\Lambda = 0.7$, and $H_0 = 70$ km sec $^{-1}$ Mpc $^{-1}$ (e.g. Im et al. 1997), and AB system for magnitudes.

2. DATA

2.1. The Sample

The elliptical galaxies that we study in this paper are selected from a catalog of nearby ($z < 0.05$), luminous ($M_r < -20.5$) early-type galaxies in the SDSS Stripe 82 imaging area which is located along the celestial equator in the Southern Galactic Cap ($-50^\circ < \alpha < 59^\circ, -1.25^\circ < \delta < 1.25^\circ$; Kaviraj 2010; hereafter K10). The reason why we chose the catalog is that it accompanies images that are ~ 2 magnitudes deeper than SDSS single scan images, enabling us to identify faint merging features like tidal tails for sub-classification of early-type galaxies. In K10, they classified galaxies into various morphological classes (early-type galaxies and late-type galaxies and 'Sa-like' systems which are bulge-dominated galaxies with faint spiral features) through a visual inspection of both monochromatic Stripe 82 and multi-color SDSS standard-depth image. In K10, early-type galaxies are divided further into 5 types : early-types

without any merging features, early-types with tidal features, dust features, both the dust and the tidal features, and early-types that are interacting. For our study, we regrouped the early-type galaxies into three types – 238 objects without merging features (relaxed type), 38 objects with tidal features (tidal-feature type) and 22 objects that exhibit dust features including cases showing both tidal and dust features (dust-feature type). We excluded the interacting types in K10 since the number of such object is small and they in general pose a challenge during the surface brightness fitting process. Overall, the “relaxed” early-types are considered as objects that experienced mergers long time ago so that their merging features disappeared. The “tidal-feature” early-types are considered as objects that experienced a dry merger or a wet merger relatively recently (\lesssim a few Gyrs ago) and the early-types with dust-lanes are considered as objects that experienced a wet merging recently. Figures 1 – 3 show example images of the three types of early-type galaxies.

In the next step, we cross-matched the K10 early-type galaxies with the NIR data from UKIDSS LAS. During this process, we also excluded 18 elliptical galaxies that have bright objects in the vicinity (to an extent that they cannot be masked out) since a reliable fitting of their surface brightness profiles becomes difficult under the presence of the bright neighbors. These neighbors are foreground stars or galaxies. Example images of the early-types with bright neighbors are presented in Figure 4 (the top two panels).

A visual inspection of the K10 early-type galaxies reveal objects with disks (23% of the sample). The presence of the disk makes our color gradient analysis complicated since the stellar populations in disks may significantly differ from those in bulges. Also, objects that underwent major merging events are likely to have a non-significant disk component. Therefore, we excluded early-type galaxies with a significant disk component (which we suspect mostly are S0's or S0a's). This is done by matching the K10 early-type galaxies with those in a catalog created by Simard et al. (2011) which provides the bulge to total light ratio (B/T) of SDSS galaxies from a 2-dimensional surface brightness fitting using GIM2D (Simard et al. 1999). In general, elliptical galaxies have $B/T \gtrsim 0.5$ in the optical wavelengths longer than 0.4 micron (e.g. Im et al. 2002; Simien & de Vaucouleurs 1986), therefore we select early-types with $B/T \gtrsim 0.5$, and call them “elliptical galaxies”. Most of the K10 early-type galaxies are found in the catalog of Simard et al. (2011), but some were not, because they are too bright and extended for the automated GIM2D pipeline to handle them properly. For such early-types that are not in the catalog of Simard et al. (2011), we performed a 2-dimensional surface brightness fitting using GALFIT (Peng et al. 2010), and rejected those with $B/T < 0.5$ (5 such cases; see § 3.1). See Figure 5 for disky early-types rejected by this procedure.

After the rejection of the disky early-type galaxies, 206 “elliptical” galaxies remain in the K10-LAS matched sample. Additionally 2 elliptical galaxies are excluded from the sample since they are too small (the outer boundary for the color gradient range is smaller than ~ 7 arcsec) for deriving reliable color gradients. Images

of these small early-types are given in Figure 4 (the bottom two panels). Finally, we have 162 relaxed, 32 tidal-feature and 10 dust-feature type elliptical galaxies in the final sample for our analysis as indicated in Table 1.

2.2. Optical and NIR Data

We used the SDSS Stripe 82 imaging data for the study of optical properties. The Stripe 82 data are taken from the SDSS Data Release 7 (Abazajian et al. 2009). A co-addition of about 50 SDSS single scans provides *ugriz* images ~ 2 mags deeper (SB limits of $\mu_r \sim 26$ mag arcsec $^{-2}$) than the main SDSS images of individual scan. The *g*-band and *r*-band images were downloaded from the SDSS Data Archive Server (DAS), and they were used to derive surface brightness profiles. We find that the optical band seeing is not uniform with the range of 1.0 – 1.5". This point will become important when deriving optical-NIR color gradient as we shall describe later. The pixel scale of the SDSS images is 0.3961"

For the NIR images, we used the Data Release 8 of UKIDSS LAS (Lawrence et al. 2007). Most but not all of the SDSS Stripe 82 region was covered ($-25^\circ < \alpha < 60^\circ$, $-1.25^\circ < \delta < 1.25^\circ$) in *YJHK*-bands by UKIDSS LAS. Typical seeing of an LAS image is 1" FWHM in *K*-band. The depth of the UKIDSS LAS data is shallower than the SDSS Stripe 82 data (SB limit is $\mu_K \simeq 20$ mag arcsec $^{-2}$), so the fitting range for an optical-NIR color gradient is limited by the NIR data. We limited ourselves to the use of only *K*-band data, since *K*-band provides the maximal wavelength baseline in conjunction with the optical bands, and the use of *J* or *H*-bands appear redundant for the stellar population analysis (e.g. Gil de Paz & Madore 2002). Although inclusion of more passbands, especially those in UV, is likely to improve the analysis, we limit ourselves to the use of *g*, *r*, and *K*-band data for simplicity here. The *K*-band images of our sample galaxies are downloaded from the WFCAM science archive³. The pixel size of an LAS image is 0.4", comparable to but a bit larger than the pixel size of the SDSS images.

3. ANALYSIS

3.1. Surface Brightness Profile

In order to investigate color/age/metallicity gradients, we derived SB profiles of each elliptical in *g*, *r*, and *K* (see Figure 1 – 5). The first step in the SB profile fitting is to estimate a proper background, and to subtract it from the images. This is because, in the outer parts of galaxies where the sky noise is dominant, SB can change substantially depending on the value of the sky background. Therefore, the background subtraction is very important in the analysis of color gradients and the derivation of SB at the outer region of galaxies. Both the SDSS Stripe 82 and the UKIDSS LAS data offer sky background estimates in each image, however we find that these values are only approximately accurate. Hence, we re-estimated sky background of each image with a growth curve analysis. We carried out the growth curve analysis in the following way. The initial guess of the background is obtained from sky value indicated in the FITS image

header. The initial guess is subtracted from the image, and the growth curve is constructed using the IRAF ELLIPSE task. We examined the growth curve out to $\sim 2 \times$ the isophotal radius of the object (typically, 15 – 40 arcsec in radius, with isophote at 1.5- σ of the sky noise), and a small amount of background value was added or subtracted manually until the background become flat at such a radius. Through this process, we determine the sky background value to an accuracy of $\sim 0.03\%$.

After subtracting the background, we used the IRAF ELLIPSE task to fit the SB profile. We fitted the *r*-band images first in order to use the *r*-band results as a reference to compare with the other band data, because the photometric sensitivity of the *r*-band is highest among the SDSS filters (Gunn et al. 1998). We fixed the center position as the position that is computed by ELLIPSE, and the position angle and the ellipticity are set free. In some cases, elliptical galaxies exhibit a twist of isophotes in position angle and ellipticity as a function of radius, therefore fixing these two parameters to single values often result in a poor fitting of the SB profile with the ELLIPSE model. We set a step size for the radial increase to be $1.5 \times$ the previous radius of an isophote with the starting radius of 2 pixels (0.8"). The non-linear increase of the isophotal radius allows us to match S/N of the outer isophotes to the inner ones. Once the fitting of the *r*-band images is done, we fitted the *g*-band and the *K*-band images using the best-fit ELLIPSE parameters from the *r*-band image. Since the *r*-band images have a slightly different pixel scale and a position angle in comparison to the *K*-band images (in some cases), we modified the radial steps (in pixel) and the position angle values for the *K*-band ELLIPSE parameters before fitting the *K*-band images to match those of the *r*-band fits. Objects in the vicinity of an elliptical galaxy were masked out by using the positional information from SExtractor (Bertin & Arnouts 1996). Some objects that are not separated from the elliptical galaxy were masked out manually during the ELLIPSE fitting process. Also masked out were dust features in dust-feature type ellipticals. Figure 6 shows examples of the masking of the neighbor objects. Some of the dust-feature type ellipticals have more than 50% of pixels masked out when the masking was done conservatively (i.e., many pixels outside the dust features were also masked). To see if this affected the SB-fitting significantly, we varied the fraction of pixels to be masked out by decreasing it to 30% level and performing SB fittings to such images. We did not find a strong change in the derived SB profile through this exercise (See Figure 7). Finally, SB profiles were constructed along the major axis of each ellipse. Figures 1 – 5 show examples of the SB fitting, together with *r*- and *K*-band images of elliptical galaxies. The derived total *K*-band magnitudes and the major-axis effective radii r_{eff} in *K* and *r* from the fitting are presented in Table 5.

3.2. Color Gradients

Color profiles were obtained by subtracting a SB profile in one band from a SB profile in another band. As the SDSS and the UKIDSS/LAS images have different pixel scales, we linearly interpolated isophotal radii of the *K*-band data in $r^{1/4}$ scale, because elliptical galaxies are known to have nearly linear SB profiles in logarithmic

³ <http://surveys.roe.ac.uk/wsa>

scale as a function of $r^{1/4}$ (de Vaucouleurs' law). Color gradient slopes were obtained by a least square fitting of a 1st order polynomial to the color profiles divided by the logarithmic radius scale in units of r_{eff} as given in Eqs. (1) – (3). The mpfit of Interactive Data Language (IDL) is used for the linear fit (Markwardt 2009).

$$\nabla_{g-r} = \frac{\Delta(\text{SB}(g) - \text{SB}(r))}{\Delta \log(r/r_{eff}(r))} \quad (1)$$

$$\nabla_{r-K} = \frac{\Delta(\text{SB}(r) - \text{SB}(K))}{\Delta \log(r/r_{eff}(K))} \quad (2)$$

$$\nabla_{g-K} = \frac{\Delta(\text{SB}(g) - \text{SB}(K))}{\Delta \log(r/r_{eff}(K))} \quad (3)$$

The effective radius in K -band, $r_{eff}(K)$, was used for ∇_{r-K} and ∇_{g-K} and the $r_{eff}(r)$ was used for ∇_{g-r} . Magnitude errors of color profiles at each radius were taken as SB profile errors in two bands added in quadrature. The inner boundary of the fitting range was set to be 1.5 times the seeing FWHM of the image with the worse seeing, and the outer boundary is set to be the location where SB starts to drop below 1.5 times the background noise of the image with the shallower depth (see § 4.1). Note that we used SDSS images with regular depths (the depth comparable to UKIDSS LAS images) to check if the shallower depth of the UKIDSS LAS image affect the color gradient values. Through such an exercise, we confirm that limiting the fitting range to the depth of the shallower image does not introduce systematic bias in the color gradient measurements although uncertainties in the gradient values increase as a result of the loss of S/N. The error in the color gradient is the formal fitting error returned at the end of the least-squares fitting process. Figures 9 – 11 show examples of the $g-r$, $r-K$, and $g-K$ color profiles in three different mass (luminosity) bins, together with the color gradient values. Also, we present in Figure 12 the median $g-r$, $r-K$, and $g-K$ color profiles in three different mass (luminosity) bins, overlaid on the color gradient profiles of all the ellipticals belonging to each mass bin.

3.3. Age and Metallicity Gradients

We derived age and metallicity gradients by using a $g-r$ and $r-K$ color-color diagram. Figure 13 demonstrates the procedure used for deriving the age and the metallicity gradients, showing three example cases. We constructed an age-metallicity grid on the $g-r$ and $r-K$ diagram using a simple stellar population (SSP) model of Bruzual & Charlot (2003, hereafter BC03), The Salpeter initial mass function (IMF) and the Padova 1994 stellar evolutionary track were used for the SSP model. To derive the age and the metallicity gradients, locations of the points on a color profile are plotted on the color-color diagram. By doing a bilinear interpolation on the age-metallicity grid, we derived the age and the metallicity for each radial point. Then, the age and the metallicity gradients were calculated in a similar way to the color gradients using the following equations. The errors for the age and the metallicity measurements were determined by a drawing 1- σ error box over each data point on the grid, and taking the largest/smallest age/metallicity

values at corners of the error box to be the upper and lower 1- σ limits.

$$\nabla_t = \frac{\Delta \log(\text{Age})}{\Delta \log(r/r_{eff}(K))} \quad (4)$$

$$\nabla_Z = \frac{\Delta \log(Z)}{\Delta \log(r/r_{eff}(K))} \quad (5)$$

Finally, we discuss how the derived age/metallicity gradients can be affected by the choice of the star formation history and the IMF. For example, a small amount of star formation may make the underlying stellar population look to be younger and more metal than they really are, if they are analyzed by an SSP model (Li et al. 2007). Figure 14 shows the age-metallicity grid in $g-r$ versus $r-K$ color-color space for three models incorporating different star formation histories (exponentially decaying star formation history and a constant burst with a burst duration of 1 Gyr) and a different IMF. As shown in Figure 14, extending the duration of the star formation activity (e.g. by adopting a longer burst period in a burst model, or τ , the exponential time scale of an exponentially decaying star formation model) would broaden the age intervals in the age-metallicity grid in the $g-r$ direction due to an enhanced contribution of younger stars to the bluer part of the spectrum. The age-metallicity grid expands in the $r-K$ direction too, but to a lesser extent than in $g-r$. On the other hand, the extended star formation activity has little effect in the metallicity grid in the color-color space. The net effect is that the extended star formation can make the age gradient substantially shallower (by a factor of a few or more in some cases) than in the analysis with the SSP model, while keeping the metallicity gradient results nearly intact.

This point is made clear in Figure 15, where we compare the age/metallicity gradients of our ellipticals calculated from different SF history models against those from the SSP model. We find that the average of the age gradient flattens by 50% going from the SSP model to the exponentially decaying SF model with $\tau = 1$ Gyr ($\nabla_t = 0.31$ to $\nabla_t = 0.17$), much less so in the average ∇_Z values. The effect of the IMF is mild in the color-color grid as discussed in (Renzini 2006; Hansson et al. 2012; Mancone & Gonzalez 2012). A bottom-heavy IMF (van Dokkum & Conroy 2010, 2011) would deform the color-color grid with respect to the Salpeter IMF prediction, but by a very small amount (< 0.1 mag in color) since low mass stars have little contribution to the integrated light of elliptical galaxies. An example is given in Figure 15 for the Chabrier IMF (Chabrier 2003), showing a non-significant change in the gradient values. Therefore, we consider that the effect of the IMF is negligible in the analysis of the age/metallicity gradient. Figures 16 – 18 show examples of age and metallicity profiles in three different mass (luminosity) bins, together with the gradient values.

4. COLOR, METALLICITY, AND AGE GRADIENTS

4.1. Color Gradient

Figure 19 shows the marginal distributions of color gradients of different types of elliptical galaxies. Also, Table 2 summarizes the median color gradients of each type of elliptical galaxies. The overall median color gradient

steepens from $\nabla_{g-r} = -0.06$ to $\nabla_{g-K} = -0.33$ as we increase the wavelength base line as we expected. The overall color gradients are in good agreement with previous measurements made by La Barbera et al. (2010).

Among different types of ellipticals, the color gradient median values are very similar between the relaxed ellipticals and the tidal-feature ellipticals. A K-S test of the color gradient distribution confirms that the relaxed types and the tidal feature types share a nearly identical distribution of color gradients in all the three colors (Table 3). This is similar to the result of Kim et al. (2012) who find no strong distinctions between the fundamental planes of relaxed and tidal feature ellipticals. On the other hand, the median color gradient of the dust-feature type ellipticals is markedly steeper than the other two types by twice to three times (Table 2). A K-S test gives less than 5 % probability that the color gradient distributions of the dust-feature ellipticals and the relaxed ellipticals are identical (Table 3). Note that we masked out the dust-features when fitting the SB profiles of the dust-feature ellipticals, in order to minimize the dust extinction affecting color gradient measurements. Therefore, we suggest that a difference in the formation and the evolution process is the origin for the discrepancy, rather than the dust extinction.

The fact that the relaxed type ellipticals and the tidal-feature type ellipticals share a similar color gradient distribution means that they share a similar merging history. The steep color gradient in the dust-feature types is in agreement with the expected steep color gradient from a monolithic collapse or a dissipative major merger with a high star formation efficiency. Therefore, we suspect that the dust-feature type ellipticals are the products of merging between gas-rich galaxies where the remaining gas producing the dust features.

In Figure 20, we present the K -band absolute magnitude (M_K) versus the color gradients in three different colors. Since M_K is closely related to the stellar mass (M_*), we also mark the stellar mass on the x-axis, where the stellar mass is computed assuming a mass-to-light ratio of 1. For a K -band mass-to-light ratio of 1, the absolute magnitudes of $M_K = -22$ and -23 mags correspond to the stellar mass of $10^{10.88}$ and $10^{11.28} M_\odot$ respectively (Drory et al. 2004). Different types of elliptical galaxies are plotted with different symbols, and the median, the error of the median, and the rms dispersion of the color gradients are indicated at each absolute magnitude bin, allowing us to understand how the color gradient changes as a function of the absolute magnitudes (or the stellar masses). At the bottom of each figure, we indicate median errors in the color gradient measurements.

If dry merging mixes up stellar population in each galaxy, a naive expectation is that the color gradients become shallower and the dispersion becomes smaller toward the brighter magnitude. However, Figure 20 shows that the median values of the color gradients are nearly constant as a function of absolute magnitude, somewhat in contrary to the naive expectation (possibly with an exception at the brightest end). On the other hand, the dispersion of the color gradients appears to decrease at the brighter end, consistent with the expectation. A similar trend is evident in Figure 12 too. However, the steady decrease in the scatter is illusionary and reflects the larger measurement errors as discussed below.

To examine this trend more closely, we plot the intrinsic scatter of the color gradients as a function of K -band absolute magnitude in Figure 21. Note that the measurement errors add noises to the intrinsic scatter, therefore we subtracted the contribution of the measurement errors from the observed scatter to obtain the intrinsic scatter as described below. Note that the subtraction of the measurement errors is more important at the faint end than at the bright end since faint objects have large color gradient errors due to the lack of data points to fit for their SB. We assumed that the color gradients are distributed in Gaussian with its mean value equal to the measured median value of the color gradient with a certain intrinsic dispersion. Then, we constructed the measurement error distribution for actual measurement errors. We took a median value of the measurement errors (at each absolute magnitude bin), and subtracted it from the observed rms scatter to obtain an initial guess for the intrinsic scatter. In the next step, we randomly picked color gradients from the normal distribution of the color gradients, assigning measurement errors to each value by randomly picking a measurement error from the measurement error distribution that we constructed earlier. The median value and the rms scatter are computed from this simulated set of color gradients. The rms scatter was compared with the observed rms scatter, and the value of the intrinsic scatter was adjusted if the rms scatter from the simulation does not match the observed rms scatter. Finally, after iterations of the above process, we determined the intrinsic scatter to be the intrinsic scatter in the simulation where the rms scatter of the simulation is identical to the observed rms scatter.

Error of the intrinsic scatter of color gradients, σ_x , was estimated by propagating the color gradient measurement errors in the following way. Here, x is the intrinsic scatter, N is the number of galaxies in a certain magnitude bin, a_i is the color gradient value of the i 'th galaxy, σ_{a_i} is the measurement error of the color gradient of the i 'th galaxy, and μ is the average of the color gradients. The values of the scatters are presented in Table 4 and shown in Figure 21. Although the estimates of the error values are mathematically sound, we caution that the error estimates do not include potential systematic effects discussed in Section 3.3, and may be under- or over-estimated due to small number statistics in some of the bins.

$$x = \sqrt{\frac{\left(\sum_{i=1}^N a_i^2\right)}{N} - \left(\frac{\sum_{i=1}^N a_i}{N}\right)^2} \quad (6)$$

$$\sigma_x^2 = \sum_{i=1}^N \sigma_{a_i}^2 \left(\frac{\partial x}{\partial a_i}\right)^2, \quad \frac{\partial x}{\partial a_i} = \frac{a_i - \mu}{Nx} \quad (7)$$

$$\sigma_x = \sqrt{\sum_{i=1}^N \sigma_{a_i}^2 \left(\frac{a_i - \mu}{Nx}\right)^2} \quad (8)$$

In Figure 21, we find that the steady decrease of the rms scatter toward the massive end disappears for the optical-NIR color gradients when the intrinsic scatter is considered. The decrease in the intrinsic scatter is only

visible at the most massive end at a few σ level. The implication of the result will be discussed later, in relation to the merging activity (§5).

4.2. Age and Metallicity Gradients

Our analysis (§ 3.3) allows us to derive age and metallicity gradients. The results of the age and the metallicity gradient are described in this section.

Figure 22 shows the marginal distribution of the age and the metallicity gradients. As was the case for the color gradients, the relaxed type ellipticals and the tidal-feature type ellipticals share a nearly identical distribution, with a positive age gradient ($\nabla_t \simeq 0.2$) and a negative metallicity gradient ($\nabla_Z \simeq -0.4$). The dust-feature type ellipticals have small age gradients (except for two outliers), and significantly steep metallicity gradients of $\nabla_Z \simeq -0.8$. The very steep metallicity gradient of dust-feature type ellipticals supports the idea that they are the products of wet merging events.

The derived mean ∇_Z is steeper than ∇_Z values derived from studies that are based on the line indices ($\nabla_Z \sim -0.2 - -0.3$; Ogando et al. 2005; Spolaor et al. 2010; Rawle et al. 2010; Sánchez-Blázquez et al. 2007; citealtani07), but is in agreement with the values in La Barbera et al. (2010) and Tortora & Napolitano (2012) that are based on color profile analysis like our study. The origin of the discrepancy is unclear although a slightly positive age gradient in the color gradient analysis steepens the metallicity gradient but not to the extent that it resolves the difference. The line indices analysis that derive the flatter ∇_Z assume $\nabla_t = 0$ or find null ∇_t . While the line indices studies are limited at $r < r_{eff}$, the color gradient studies are done out to a few $\times r_{eff}$, so this may be the cause of the discrepancy.

The absolute values of the gradients are quantities that are subject to the analysis methods (e.g., the adopted stellar population synthesis models, see Li et al. 2007) so that we caution readers not to pay too much attention to the absolute values but concentrating on the relative changes in the gradients.

In Figure 23, we show the M_K versus the age and the metallicity gradients. With the thick points, we indicate the median ∇_t and ∇_Z values and their errors. On these points, the thin error bars show the rms dispersion. The thick error bars represent the errors of the median, which are derived by dividing the rms dispersion by \sqrt{N} where N is the number of objects in the corresponding bin. Like the color gradients, the age and the metallicity gradients do not show a significant change as a function of M_K . One exception is the brightest bin (corresponding to the stellar mass of $\sim 5 \times 10^{11} M_\odot$) where both ∇_t and ∇_Z start to flatten. However this trend at the brightest bin should be taken with a caution since only six objects are included in the bin.

Just like the color gradients, this result is consistent with a similar analysis performed by La Barbera et al. (2010). On the other hand, La Barbera et al. (2010) do not show a result at the very massive end of $\sim 5 \times 10^{11} M_\odot$, so the flattening of the age and the metallicity gradients at the brightest bin is not noticed in their work. The flattening of the age and the metallicity gradients at the brightest end is interesting since this is exactly what is expected if these ellipticals underwent frequent

dry merging. Obviously, more number statistics at the bright end is desired to make a stronger case for this.

Similarly to the color gradients, the scatters in the age and the color gradients appear to decrease at the brightest magnitude bin. As a closer examination of this trend, we show in Figure 24 and Table 4 the intrinsic scatter of the age and the metallicity gradients as a function of the absolute magnitude. The intrinsic scatter in these gradients are obtained in an iterative process identical to the method we employed for the intrinsic scatter of color gradients (see the previous subsection). Errors of the intrinsic scatters are estimated using Eqs. (6) – (8), but here replacing the color gradients with ∇_t or ∇_Z .

The derived intrinsic rms scatter is about 0.3 at a lower mass range of $10^{10.7} M_\odot < M < 10^{11.4} M_\odot$, which is roughly in agreement with the scatter found in Ogando et al. (2005) at a similar mass range. Like the scatters of color gradients, the scatters of these quantities stay nearly constant out to $M_K \sim -23.40$ or $M \sim 10^{11.4} M_\odot$, but decreases at the most massive end by nearly a factor of two per a factor of two change in mass (or luminosity). The reduction in the scatter is dominated by the relaxed and the tidal-feature type ellipticals. On the other hand, the reduction in the scatter is inverted for the tidal-feature type ellipticals, although the larger errors in the scatter (due to the smaller number of galaxies available) for these types of objects make it difficult to draw a firm conclusion.

Overall, the two evidences – the possible flattening of the age and the metallicity gradients and the decrease in the scatter of these gradients at the most massive end – are in agreement with the expectation of what would happen under dry merging, and this point will be discussed in more detail below.

5. IMPLICATION ON DRY MERGING

5.1. Model

In the previous section, we saw that the scatters in the color/age/metallicity gradients decrease at the brightest M_K . Here, we present a simple model that calculates how the metallicity gradient would change as a function of absolute magnitude and mass if major dry merging is the dominant mechanism for the growth of elliptical galaxies at the massive end.

To do so, we use a simulation result from Di Matteo et al. (2009) where they perform simulations of major dry merging of elliptical galaxies with various initial conditions, and present the metallicity gradients of pre-mergers and merger products. Borrowing their results, we establish a relation between the average metallicity gradients of two galaxies before merging, and the metallicity gradient of the merger product (Figure 25). We find that there is a good correlation between the average of the metallicity gradients of pre-merging galaxies ($(\nabla_Z(gal1) + \nabla_Z(gal2))/2$) and the metallicity gradient of the merger product ($\nabla_Z(merger)$) as

$$\nabla_Z(merger) = 0.55 \times \frac{\nabla_Z(gal1) + \nabla_Z(gal2)}{2} - 0.02. \quad (9)$$

The relation shows that the metallicity gradient flattens on average when two galaxies merge, with the resulting ∇_Z being about 60 % of the average value of the ∇_Z 's

of the two pre-merging galaxies. The correlation is reasonably tight, with the largest rms dispersion of 0.03 in $\nabla_Z(\text{merger})$. This dispersion is sufficiently smaller than the reduction in the metallicity gradient value (which is order of 0.1), therefore we ignore the dispersion in Eq. (9) in the following discussion.

Two consequences are expected from Eq. (9). One is that the metallicity gradient flattens gradually as the masses of ellipticals increase in a dry merging dominated evolution. Roughly speaking, there should be a decrease in the metallicity gradient by a factor of 0.55, over a mass doubling scale (0.3 dex in $\log(M)$). Another consequence is the decrease of the scatter in the color and the stellar population gradients at a high mass end. Suppose that we have a variety of the stellar population gradients for pre-merging ellipticals. If we randomly merge galaxies with different metallicity gradients, the merging averages the metallicity gradient values and remove galaxies with extreme metallicity gradients. Since the merger product will be more massive than each of its predecessors, we expect that the major dry merging would reduce the scatter in the color gradients at high mass end.

To see how the mean ∇_Z and its intrinsic scatter would evolve under dry merging, we performed a simple simulation. Here, we assumed an initial distribution of ∇_Z in Gaussian with its mean value at $\nabla_Z = -0.4$ and the intrinsic scatter at $\sigma_{\nabla_Z} = 0.3$. These values correspond roughly to the observed mean ∇_Z and its scatter at $M = 10^{10.9} M_\odot$. We assume that a certain fraction, f_{merg} , of galaxies in a mass bin underwent dry merging. This free parameter f_{merg} will control the amount of change in the mean metallicity gradient and its scatter.

Figure 26 shows the result of this simulation. The metallicity gradient and its scatter change the most when f_{merg} is the largest. At $f_{\text{merg}} = 1$, the mean metallicity gradient and its scatter changes by a factor of 0.6 and 0.4 respectively, per each mass doubling. We find that this trend is independent of the initial mean ∇_Z and σ_{∇_Z} values.

Based on the simulation, we derive the following relations at $f_{\text{merg}} = 1$:

$$\Delta \log(\langle \nabla_Z \rangle) = -0.74 \Delta \log(M), \quad (10)$$

and

$$\Delta \log(\sigma_{\nabla_Z}) = -1.3 \Delta \log(M). \quad (11)$$

Here, $\Delta \log(\langle \nabla_Z \rangle)$, $\Delta \log(\sigma_{\nabla_Z})$, and $\Delta \log(M)$ are the logarithmic changes in the mean metallicity gradient, the intrinsic scatter of the metallicity gradient, and the stellar mass, respectively.

The above relations show that the change in σ_{∇_Z} is more prominent than the change in $\langle \nabla_Z \rangle$ as a result of dry merging by a factor of two.

5.2. Is Major Dry Merging Important?

With the theoretical expectations from major dry merging at hand, we now proceed to interpret our observational results about ∇_Z . Figure 27 shows the comparison of the observed change in ∇_Z and σ_{∇_Z} with a model prediction. In the figure, the error in σ_{∇_Z} is estimated in the same way as the errors in the scatter of the color gradient values as described in Section 4.2 and using

Eq. (8). The model plot assumes no major dry merging at $M < 10^{11.3} M_\odot$, $f_{\text{merg}} = 0.3$ at $M = 10^{11.4} M_\odot$, and $f_{\text{merg}} = 0.9$ at $M = 10^{11.6} M_\odot$.

As we have shown earlier, the reduction in σ_{∇_Z} is observed at the massive end ($> 10^{11.4} M_\odot$). The major dry merging can provide an explanation for this result. The observed reduction in the scatter is about 0.1 over the mass increase of 0.4 dex, and according to Figure 26, this can be achieved by assuming that 70 – 100 % of ellipticals at the higher mass bin have experienced major dry merging while the rest went through the formation mechanisms similar to those at the lower mass bins (i.e., they possess similar ∇_Z and ∇_t distributions to those at the lower mass bin). The possible formation and the evolution mechanisms at the lower mass bin include the wet merging, the minor merging, and the monolithic collapse (see discussions below).

According to our model, this amount of major dry merging needs to flatten ∇_Z by 0.15 over a mass doubling scale. This value is rather small compared to the change in the scatter, but should be detectable with a sufficient number of objects. At the moment, we find such a trend, but with a rather large error bar. In comparison to other works, our results are in agreement with Roche et al. (2010) where they find a reduced scatter in color gradients of BCGs. Also note that some other studies report a flattening of the metallicity gradient at the massive end (e.g., Spolaor et al. 2010).

While we find a supporting evidence for major dry merging at the high mass end, major dry merging is probably not a main mechanism driving the evolution of lower mass ellipticals with $M < 10^{11.4} M_\odot$. Between $M = 10^{10.7} M_\odot$ and $M = 10^{11.4} M_\odot$, the σ_{∇_Z} values stay nearly constant. The same trend is true for the color and the age gradients. Clearly, the trend is not consistent with the expectation from the major dry merging model we presented in this paper. In order to explain the null change in the metallicity gradients, f_{merg} should be less than $\sim 20\%$. The effect of major dry merging seems negligible in the evolution of ellipticals at this mass range. The origin of the large scatter in ∇_Z at this mass range is unclear, although there are plenty of possibilities responsible for the dispersion. Minor dry merging could steepen the metallicity gradient, rather than flattening it, by distributing the merged stellar remnants in the outer region not the inner region (Bernardi et al. 2011). Dissipative collapse could create a variety of gradients depending on the star formation efficiencies how the gravitational potential is shaped for each object (Pipino et al. 2010). Minor merging with a gas-rich galaxy could place younger generation stars at central or outer regions, making galaxies blue at certain areas and complicating the analysis of the result (e.g., Im et al. 2001).

6. SUMMARY

We examined the color, the age, and the metallicity gradients of 204 nearby ($z < 0.05$), massive ($M_r < 20.5$ mag, or $M > 10^{10.6} M_\odot$) elliptical galaxies (early-type galaxies with $B/T > 0.5$), divided into three morphological types – the relaxed, the tidal-feature, and the dust-feature types. The subdivision of elliptical galaxies was possible by using the SDSS Stripe 82 images which goes about 2 mag deeper than regular SDSS im-

ages, and the derivation of the age and the metallicity gradients was done by adding K -band data of the UKIDSS LAS to the SDSS data which enabled us to break the age-metallicity degeneracy. No significant difference is found between relaxed and tidal-feature types in the gradient properties. However, the dust-feature type ellipticals have steeper color gradients which seem to originate from wet merging rather than the dust extinction effect. The gradient values of elliptical galaxies are found to be nearly constant over the explored mass range, but we find that the intrinsic scatter of ∇_Z decreases at $M > 10^{11.4} M_\odot$ by about 0.1.

To interpret our results, we constructed a simple model that describes changes in ∇_Z and σ_{∇_Z} as a function of mass under major dry merging. The model predicts that the mean ∇_Z flattens, and σ_{∇_Z} decreases as mass of an elliptical galaxy doubles as a result of major dry merging.

From the analysis of the change in ∇_Z and its scatter, we draw the following conclusions, with a caveat that the result is based on a rather small number of objects at the massive end (~ 10). First, the observed reduction in the intrinsic scatter in the M versus ∇_Z relation supports the idea that major dry merging has acted on a significant number of ellipticals at the very massive end

($M \sim 10^{11.6} M_\odot$). Second, if the reduction of the scatter in ∇_Z is indeed caused by major dry mergers, ∇_Z should flatten at the higher mass. The result from our analysis of the SDSS/UKIDSS-LAS ellipticals is consistent with this scenario at the massive end, but not conclusive. Third, at the lower mass regime ($M < 10^{11.4} M_\odot$), the major dry merging does not appear to be the dominant process in the evolution of ellipticals. At such a mass range, the mean ∇_Z is nearly constant, and the scatter in the M_* versus ∇_Z relation is large and nearly constant (~ 0.4) too, implying that various physical mechanisms are responsible for the large scatter.

This work was supported by the Creative Initiative program, No. 2010-0000712, of the National Research Foundation of Korea (NRFK) funded by the Korean government (MEST). We thank our CEOU/SNU colleagues for useful discussion.

This paper uses the data taken with the United Kingdom Infrared Telescope (UKIRT) which is operated by the Joint Astronomy Centre on behalf of the Science and Technology Facilities and from the Sloan Digital Sky Survey project.

REFERENCES

- Abazajian, K. N., Adelman-McCarthy, J. K., Agüeros, M. A., et al. 2009, *ApJS*, 182, 543
- Annibali, F., Bressan, A., Rampazzo, R., Zeilinger, W. W., & Danese, L. 2007, *A&A*, 463, 455
- Barnes, J. E., & Hernquist, L. 1992, *ARA&A*, 30, 705
- Baum, W. A. 1959, *PASP*, 71, 106
- Bell, E. F., & de Jong, R. S. 2000, *MNRAS*, 312, 497
- Bell, E. F., & de Jong, R. S. 2001, *ApJ*, 550, 212
- Bernardi, M., Roche, N., Shankar, F., & Sheth, R. K. 2011, *MNRAS*, 412, L6
- Bertin, E., & Arnouts, S. 1996, *A&AS*, 117, 393
- Bruzual, G., & Charlot, S. 2003, *MNRAS*, 344, 1000
- Carlberg, R. G. 1984, *ApJ*, 286, 416
- Chabrier, G. 2003, *PASP*, 115, 763
- Daddi, E., Renzini, A., Pirkzal, N., et al. 2005, *ApJ*, 626, 680
- Di Matteo, P., Pipino, A., Lehnert, M. D., Combes, F., & Semelin, B. 2009, *A&A*, 499, 427
- Djorgovski, S., & Davis, M. 1987, *ApJ*, 313, 59
- Drory, N., Bender, R., Feulner, G., et al. 2004, *ApJ*, 608, 742
- Eggen, O. J., Lynden-Bell, D., & Sandage, A. R. 1962, *ApJ*, 136, 748
- Franx, M., & Illingworth, G. 1990, *ApJ*, 359, L41
- Gil de Paz, A., & Madore, B. F. 2002, *AJ*, 123, 1864
- Gunn, J. E., Carr, M., Rockosi, C., et al. 1998, *AJ*, 116, 3040
- Hansson, K. S. A., Lisker, T., & Grebel, E. K. 2012, *MNRAS*, 427, 2376
- Hinkley, S., & Im, M. 2001, *ApJ*, 560, L41
- Hopkins, P. F., Cox, T. J., Dutta, S. N., et al. 2009, *ApJS*, 181, 135
- Hwang, H. S., Geller, M. J., Diaferio, A., & Rines, K. J. 2012, *ApJ*, 752, 64
- Im, M., Griffiths, R. E., & Ratnatunga, K. U. 1997, *ApJ*, 475, 457
- Im, M., Griffiths, R. E., Naim, A., et al. 1999, *ApJ*, 510, 82
- Im, M., Faber, S. M., Gebhardt, K., et al. 2001, *AJ*, 122, 750
- Im, M., Simard, L., Faber, S. M., et al. 2002, *ApJ*, 571, 136
- Jun, H. D., & Im, M. 2008, *ApJ*, 678, L97
- Kaviraj, S. 2010, *MNRAS*, 406, 382
- Kaviraj, S., Ting, Y.-S., Bureau, M., et al. 2012, *MNRAS*, 423, 49
- Kawata, D., & Gibson, B. K. 2003, *MNRAS*, 340, 908
- Kim, T., Sheth, K., Hinz, J. L., et al. 2012, *ApJ*, 753, 43
- Ko, J., & Im, M. 2005, *Journal of Korean Astronomical Society*, 38, 149
- Ko, J., Im, M., Lee, H. M., et al. 2009, *ApJ*, 695, L198
- Ko, J., Im, M., Lee, H. M., et al. 2012, *ApJ*, 745, 181
- Kobayashi, C. 2004, *MNRAS*, 347, 740
- Kuntschner, H., Emsellem, E., Bacon, R., et al. 2010, *MNRAS*, 408, 97
- La Barbera, F., De Carvalho, R. R., De La Rosa, I. G., et al. 2010, *AJ*, 140, 1528
- Larson, R. B. 1974, *MNRAS*, 166, 585
- Lawrence, A., Warren, S. J., Almaini, O., et al. 2007, *MNRAS*, 379, 1599
- Lee, J. H., Lee, M. G., & Hwang, H. S. 2006, *ApJ*, 650, 148
- Li, Z., Han, Z., & Zhang, F. 2007, *A&A*, 464, 853
- Mancone, C. L., & Gonzalez, A. H. 2012, *PASP*, 124, 606
- Markwardt, C. B. 2009, *Astronomical Data Analysis Software and Systems XVIII*, 411, 251
- Naab, T., & Trujillo, I. 2006, *MNRAS*, 369, 625
- Ogando, R. L. C., Maia, M. A. G., Chiappini, C., et al. 2005, *ApJ*, 632, L61
- Pahre, M. A., Djorgovski, S. G., & de Carvalho, R. R. 1995, *ApJ*, 453, L17
- Peletier, R. F., Davies, R. L., Illingworth, G. D., Davis, L. E., & Cawson, M. 1990, *AJ*, 100, 1091
- Peng, C. Y., Ho, L. C., Impey, C. D., & Rix, H.-W. 2010, *AJ*, 139, 2097
- Pipino, A., D’Ercole, A., Chiappini, C., & Matteucci, F. 2010, *MNRAS*, 407, 1347
- Rawle, T. D., Smith, R. J., & Lucey, J. R. 2010, *MNRAS*, 401, 852
- Renzini, A. 2006, *ARA&A*, 44, 141
- Roche, N., Bernardi, M., & Hyde, J. 2010, *MNRAS*, 407, 1231
- Saglia, R. P., Maraston, C., Greggio, L., Bender, R., & Ziegler, B. 2000, *A&A*, 360, 911
- Sánchez-Blázquez, P., Forbes, D. A., Strader, J., Brodie, J., & Proctor, R. 2007, *MNRAS*, 377, 759
- Scarlata, C., Carollo, C. M., Lilly, S. J., et al. 2007, *ApJS*, 172, 494
- Sheen, Y.-K., Yi, S. K., Ree, C. H., & Lee, J. 2012, *ApJS*, 202, 8
- Shim, H., Im, M., Lee, H. M., et al. 2011, *ApJ*, 727, 14
- Simard, L., Koo, D. C., Faber, S. M., et al. 1999, *ApJ*, 519, 563
- Simard, L., Mendel, J. T., Patton, D. R., Ellison, S. L., & McConnachie, A. W. 2011, *ApJS*, 196, 11
- Simien, F., & de Vaucouleurs, G. 1986, *ApJ*, 302, 564
- Spolaor, M., Kobayashi, C., Forbes, D. A., Couch, W. J., & Hau, G. K. T. 2010, *MNRAS*, 408, 272
- Tal, T., van Dokkum, P. G., Nelan, J., & Bezanson, R. 2009, *AJ*, 138, 1417
- Tamura, N., & Ohta, K. 2003, *AJ*, 126, 596

- Toomre, A. 1977, *Evolution of Galaxies and Stellar Populations*, 401
- Tortora, C., & Napolitano, N. R. 2012, *MNRAS*, 421, 2478
- Trujillo, I., Förster Schreiber, N. M., Rudnick, G., et al. 2006, *ApJ*, 650, 18
- van Dokkum, P. G. 2005, *AJ*, 130, 2647
- van Dokkum, P. G., Franx, M., Kriek, M., et al. 2008, *ApJ*, 677, L5
- van Dokkum, P. G., & Conroy, C. 2010, *Nature*, 468, 940
- van Dokkum, P. G., & Conroy, C. 2011, *ApJ*, 735, L13
- Visvanathan, N., & Sandage, A. 1977, *ApJ*, 216, 214
- White, S. D. M. 1980, *MNRAS*, 191, 1P
- Worthey, G. 1994, *ApJS*, 95, 107
- Yi, S. K., Yoon, S.-J., Kaviraj, S., et al. 2005, *ApJ*, 619, L111

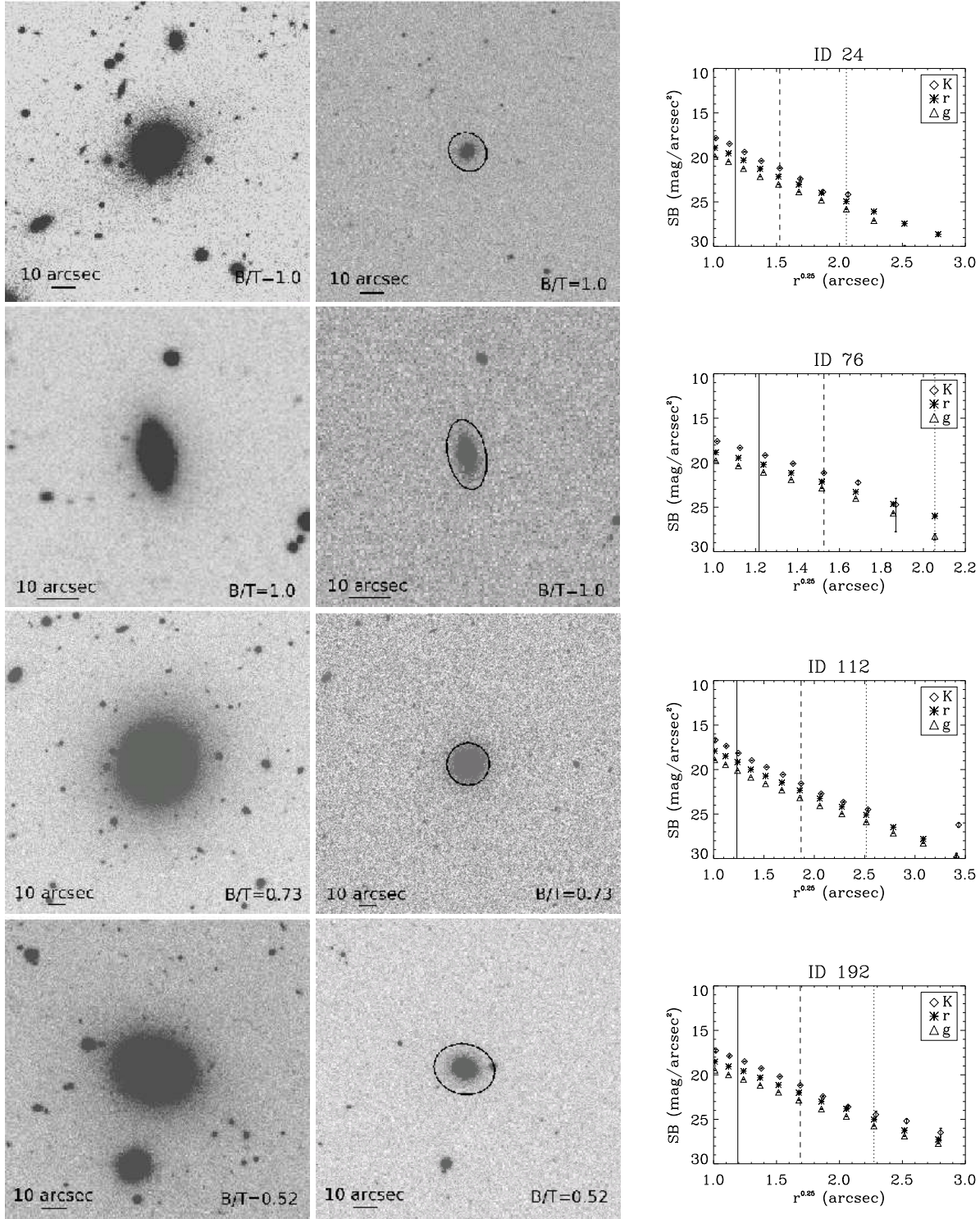


FIG. 1.— Examples of the relaxed elliptical galaxies in r -band (left), in K -band (middle) and their surface brightness profiles in g , r and K -bands (right). The scale bar and B/T in the images represent 10 arcsec and bulge to total light ratios. The vertical solid lines and the dashed lines in the plot are the inner and the outer radii for deriving $r - K$ and $g - K$ color gradients. The vertical dotted line means the outer boundary for the $g - r$ color gradient fit. The ellipses in the K -band images indicate the outer boundary for the analysis of color profiles for the K -band. The ID on top of the SB profile figures indicate the ID of the objects in Kaviraj (2010) as indicated in Table 5.

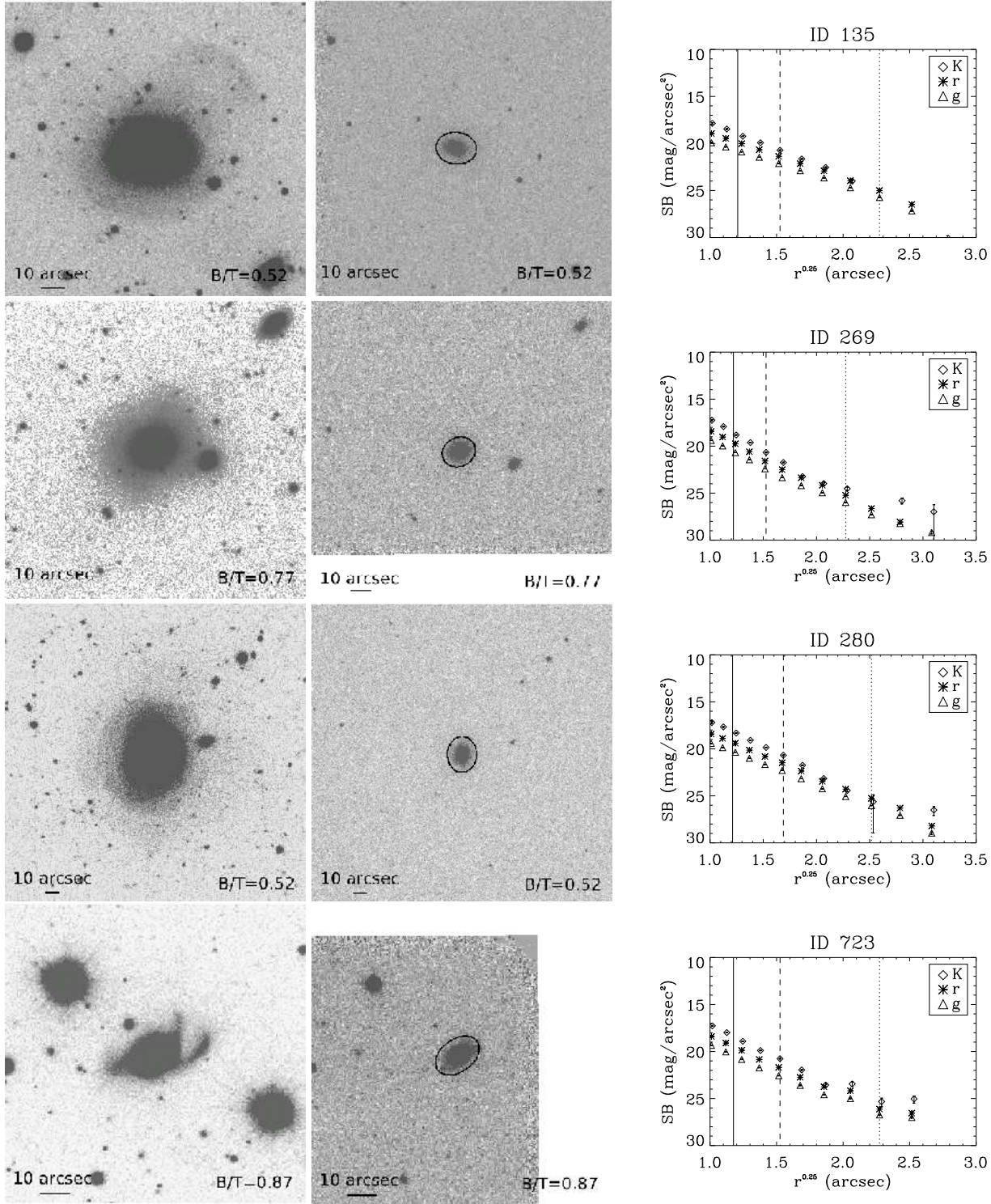


FIG. 2.— Same as Figure 1 but for tidal-feature ellipticals. Note the faint tidal features around each elliptical, which are indicative of their past merging activities.

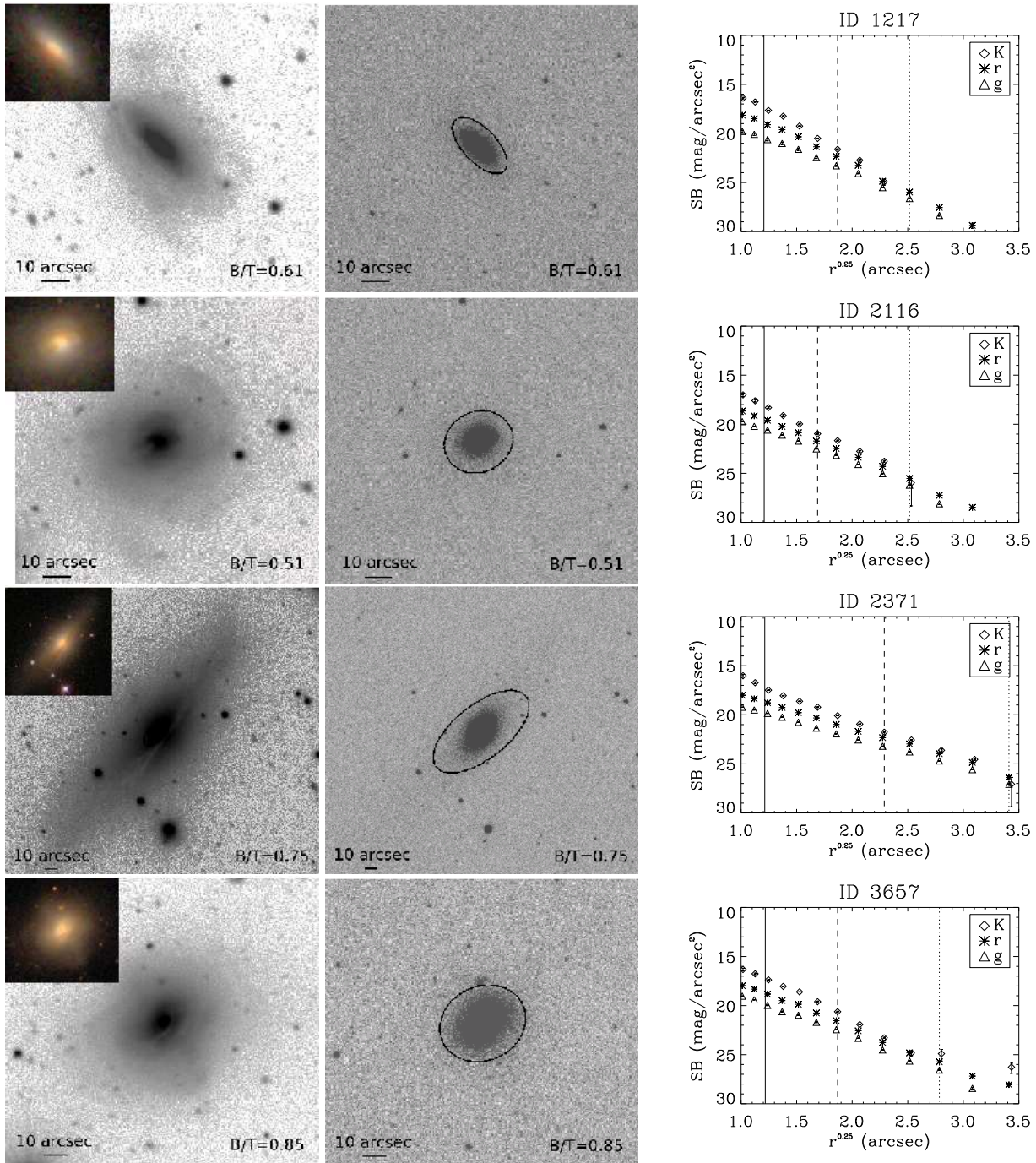


FIG. 3.— Same as Figure 1 but for dust-feature ellipticals. Note the dust-lanes in the r -band images.

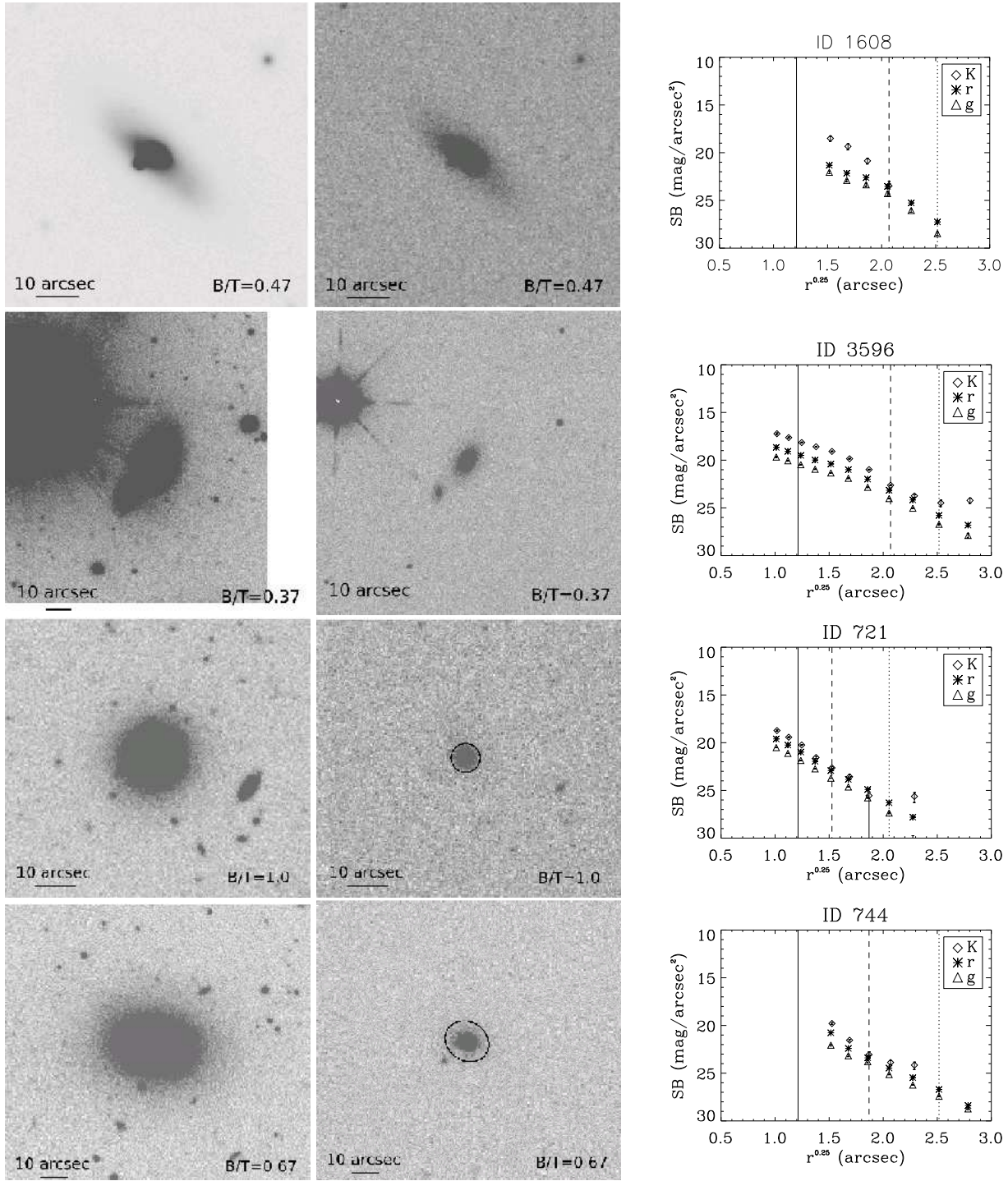


FIG. 4.— Same as Figure 1 but for the K10 early-types that are excluded from our analysis because of the presence of close neighbors (the top 2 rows) and small sizes (the bottom 2 rows).

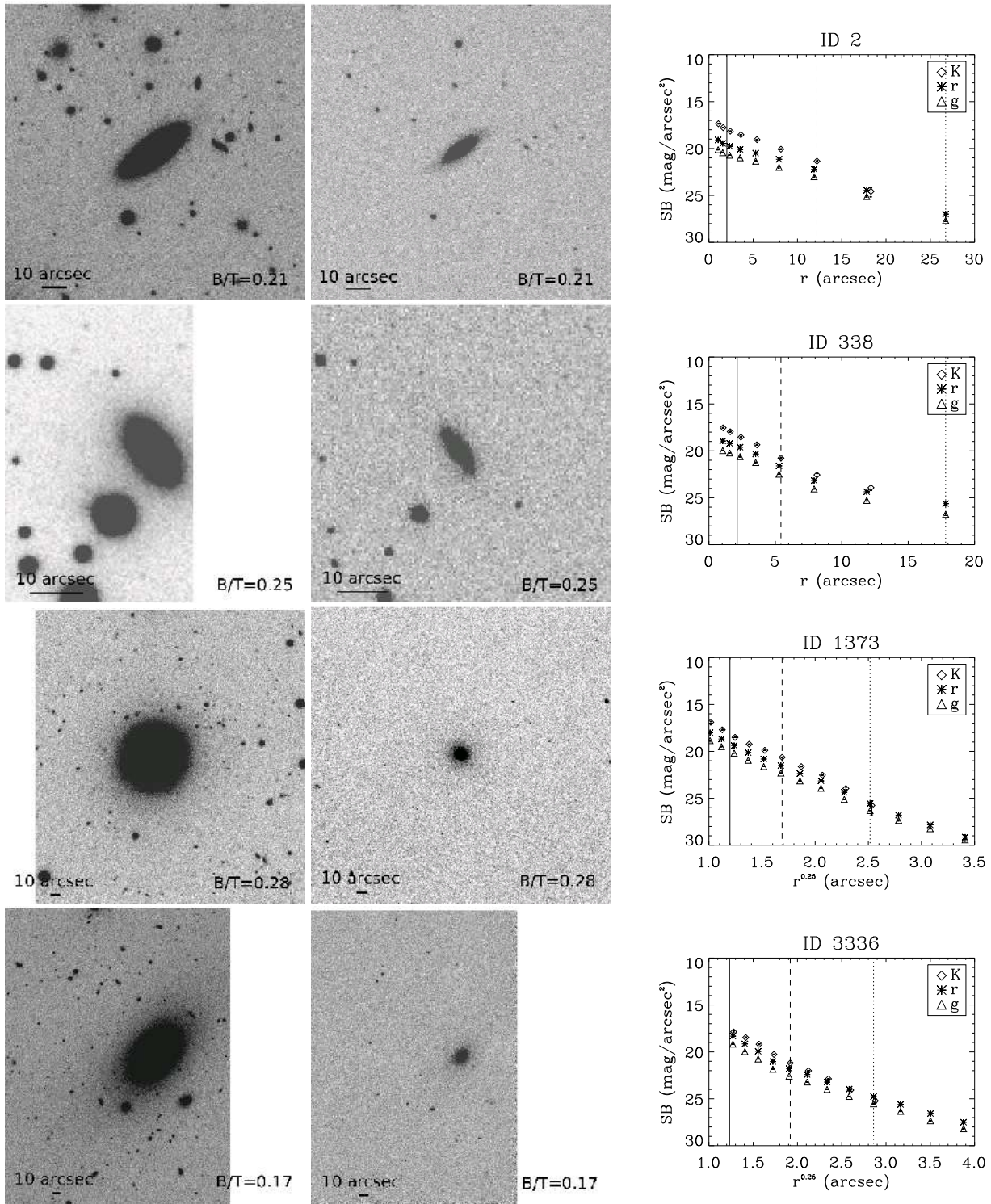


FIG. 5.— Same as Figure 1 but for the K10 early-types that are excluded from our analysis because of their low (< 0.5) B/T ratios.

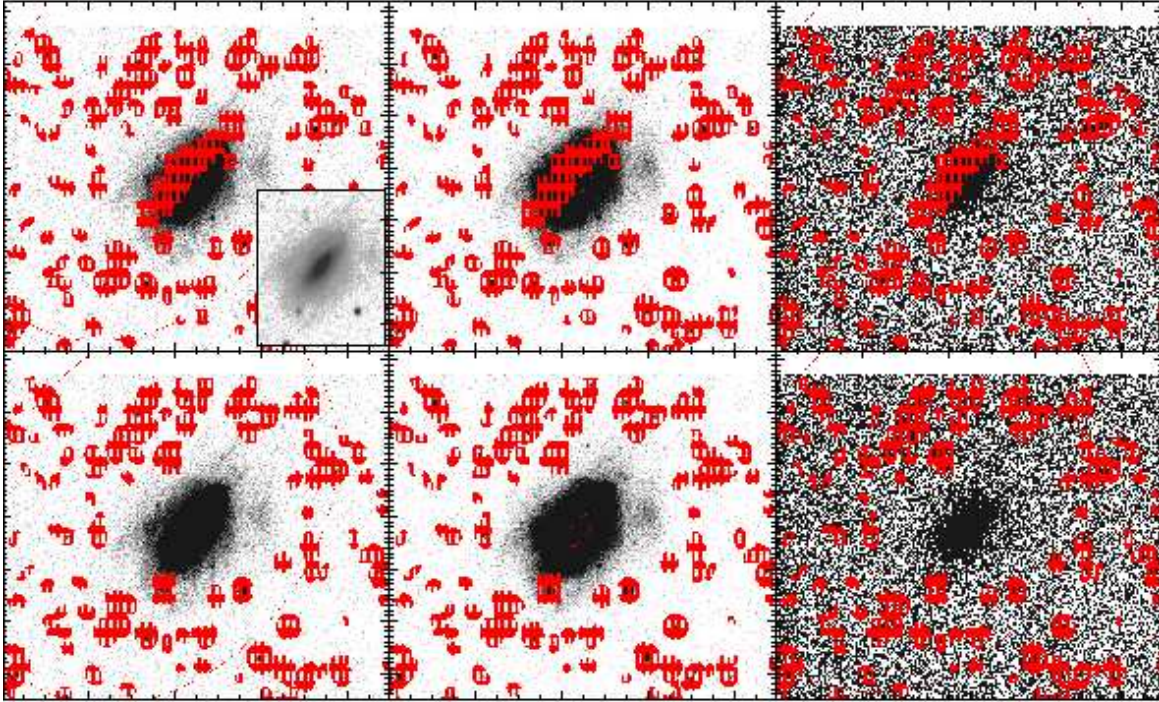


FIG. 6.— Example of masking processes during ELLIPSE fitting of elliptical galaxies (with dust lane). Top panels represent g , r and K -band images when dust lane is masked out from left to right, and the bottom panels represent the same but without masking of the dust lane.

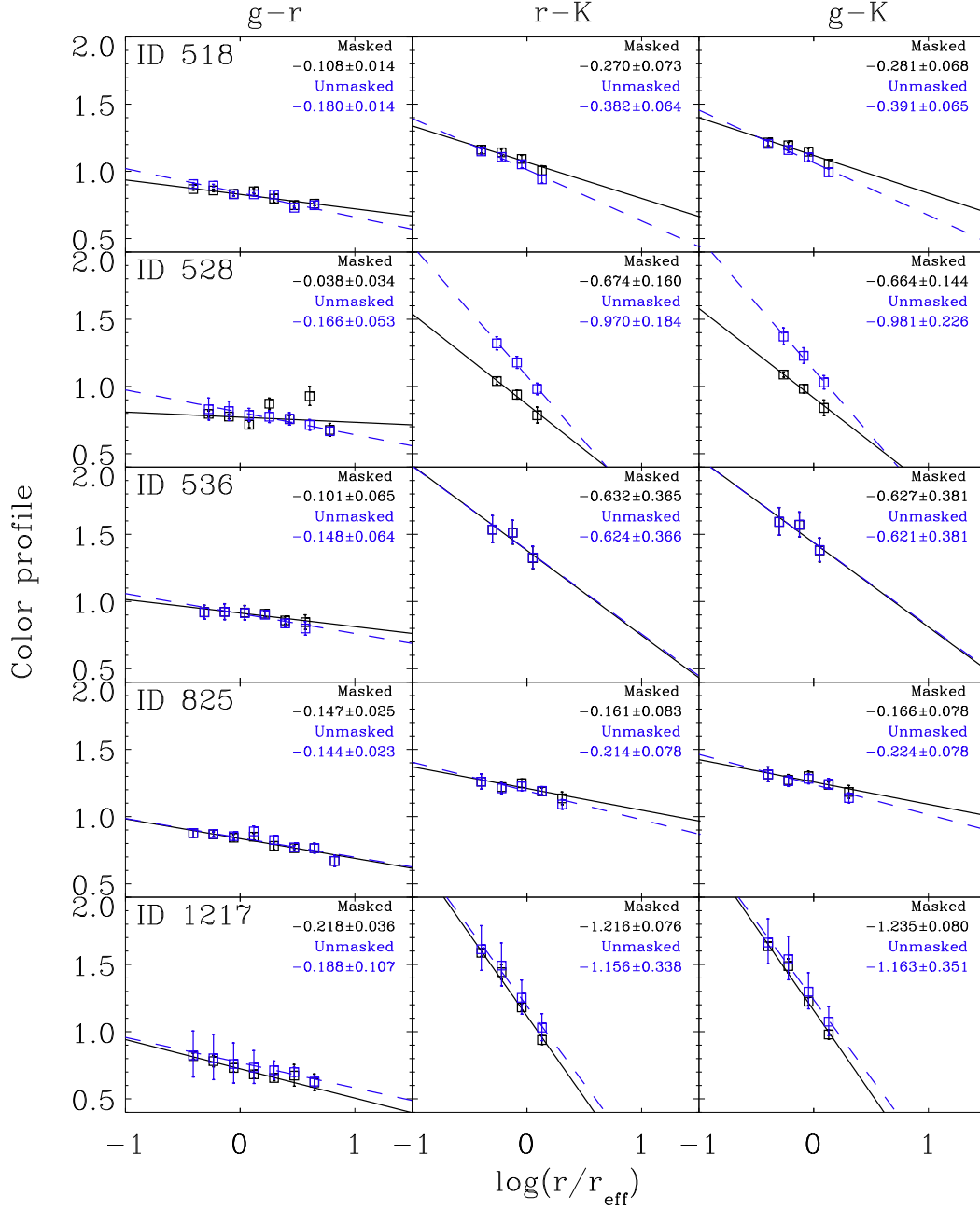


FIG. 7.— Color profiles of dust-feature elliptical galaxies in $g-r$, $r-K$ and $g-K$ from left to right. Black squares and solid lines are their color profiles after masking out dust lanes during the ELLIPSE fit. The blue squares and the dashed lines represent the cases without masking dust lanes.

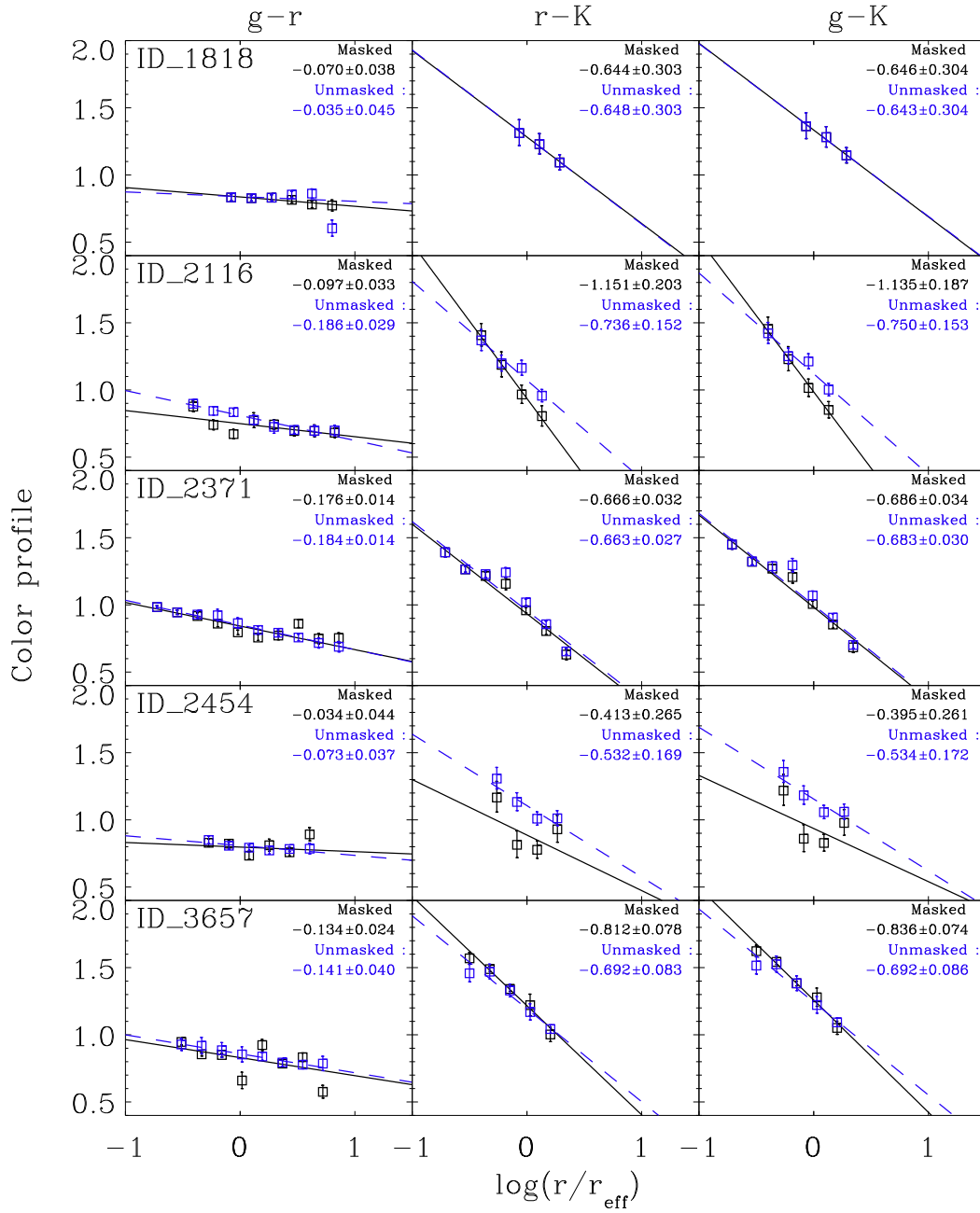


FIG. 8.— Figure 7, continued.

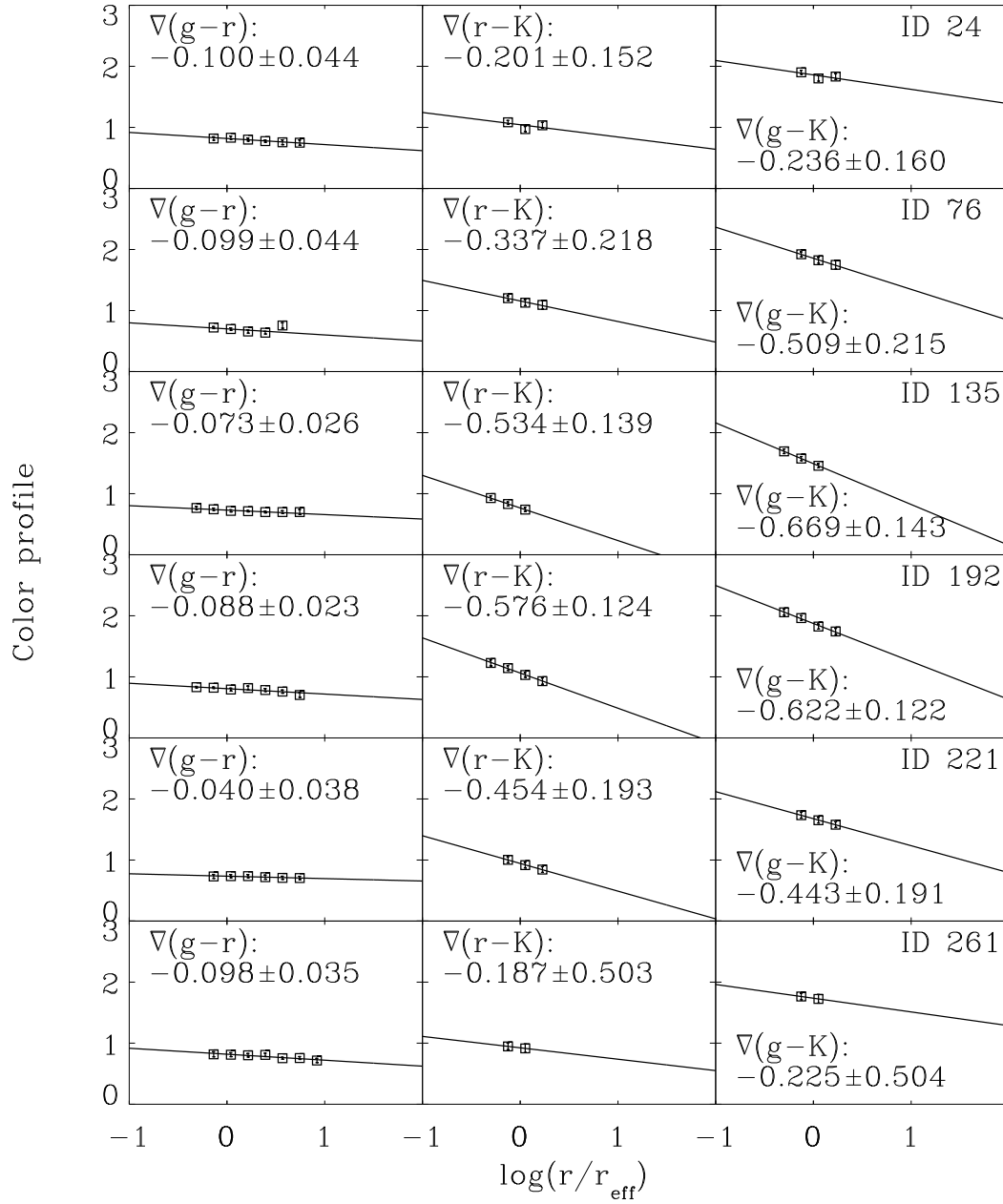


FIG. 9.— Color profiles and their color gradient values of elliptical galaxies in low-mass regime ($10^{10.6} M_{\odot} < M_{*} < 10^{10.88} M_{\odot}$). The best-fit lines are indicated for the color gradients too (the solid line).

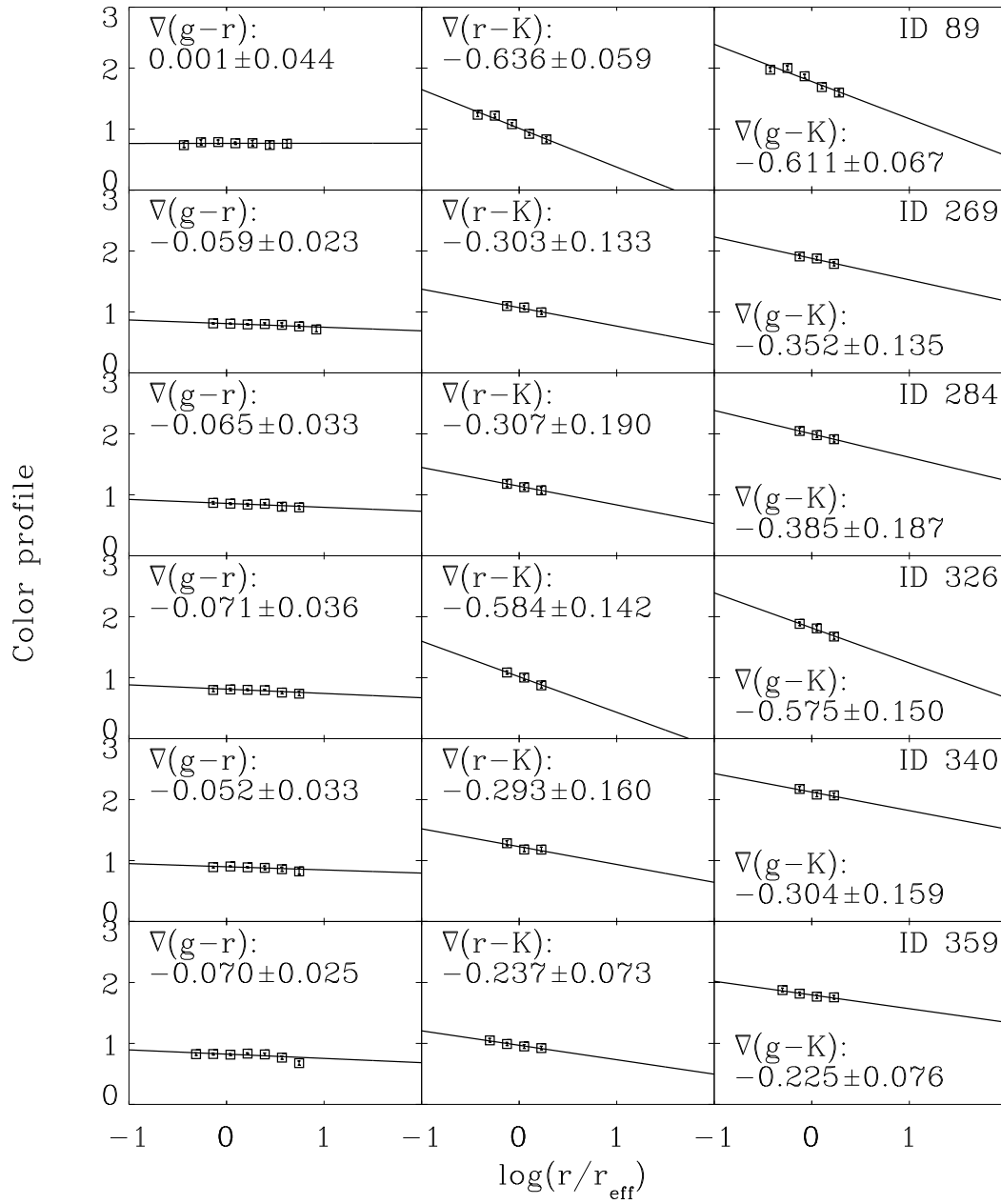


FIG. 10.— Same as Figure 9 but for elliptical galaxies in the intermediate mass regime ($10^{10.88} M_{\odot} < M_{*} < 10^{11.28} M_{\odot}$).

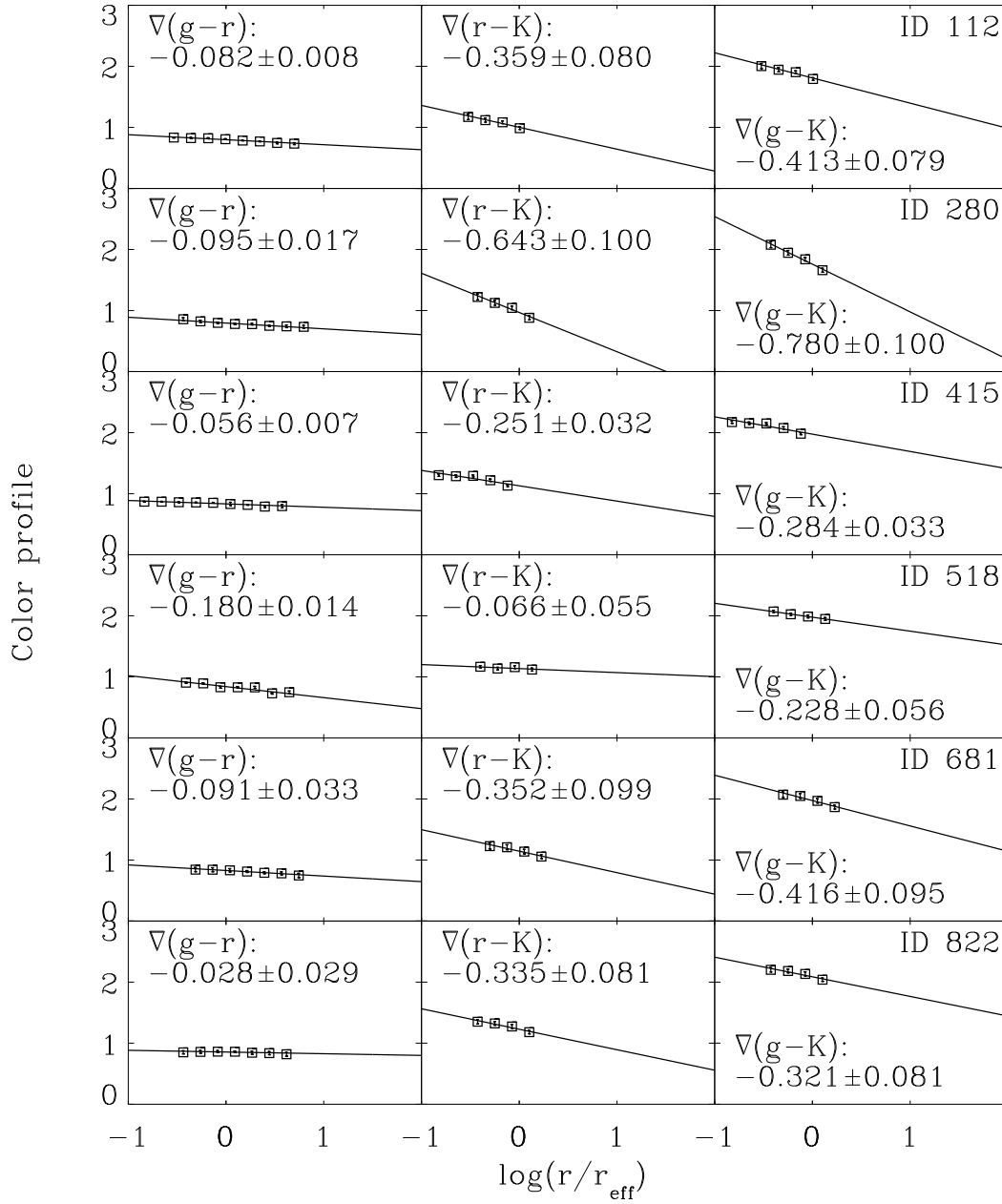


FIG. 11.— Same as Figure 9 but for elliptical galaxies in high-mass regime ($M_* > 10^{11.28} M_\odot$).

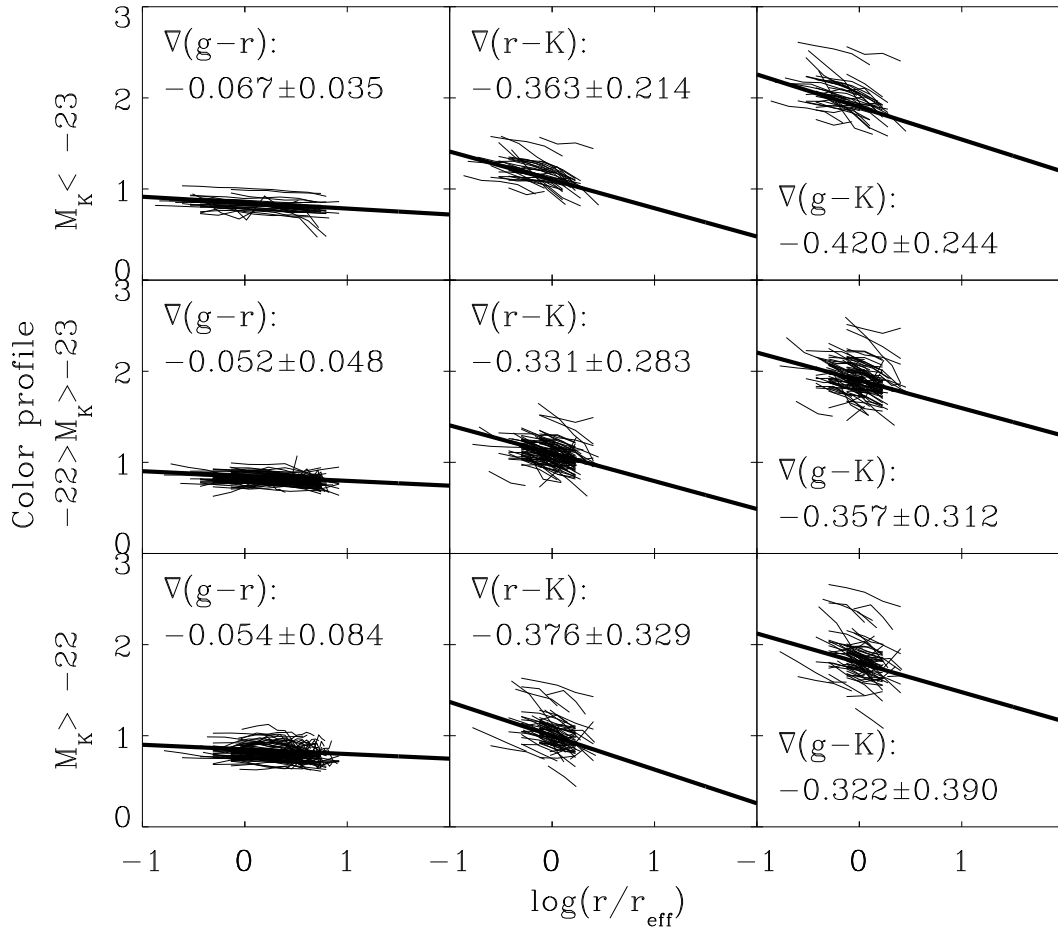


FIG. 12.— Color ($g-r$, $r-K$ and $g-K$ from left to right) profiles and median color gradients (solid line) of elliptical galaxies in high-mass regime ($M_* > 10^{11.28} M_\odot$), intermediate mass regime ($10^{10.88} M_\odot < M_* < 10^{11.28} M_\odot$) and low-mass regime ($10^{10.6} M_\odot < M_* < 10^{10.88} M_\odot$) from top to bottom.

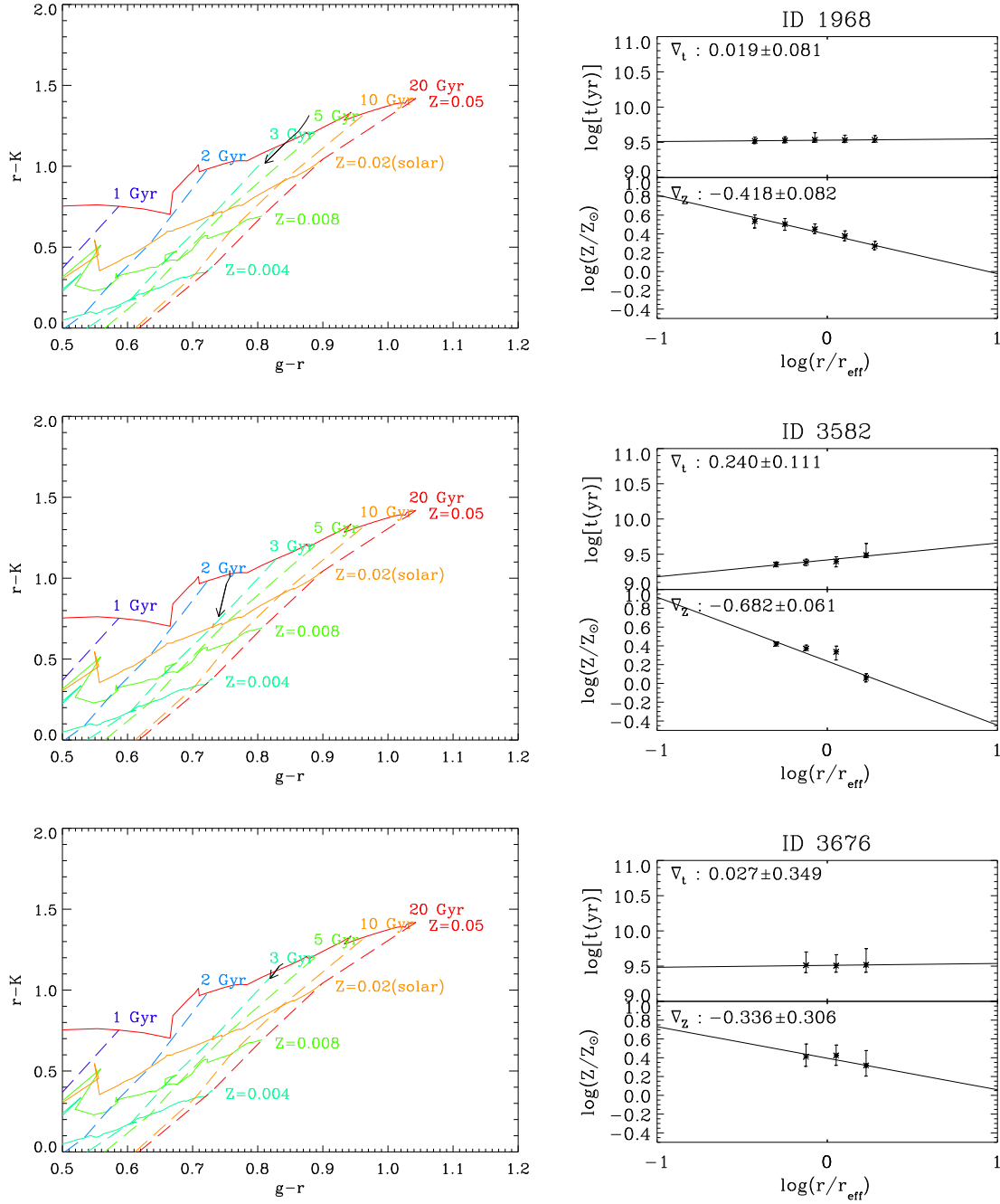


FIG. 13.— Examples showing how the age and the metallicity gradients are derived. Left: Radial changes of age and metallicity (black arrows) plotted in the $g-r$ and $r-K$ diagram. The age and the metallicity grids are created with BC03 SSP model in the manuscript. The arrow head corresponds to the outermost radius. Right: The corresponding age and metallicity profiles. Also indicated are the gradient values.

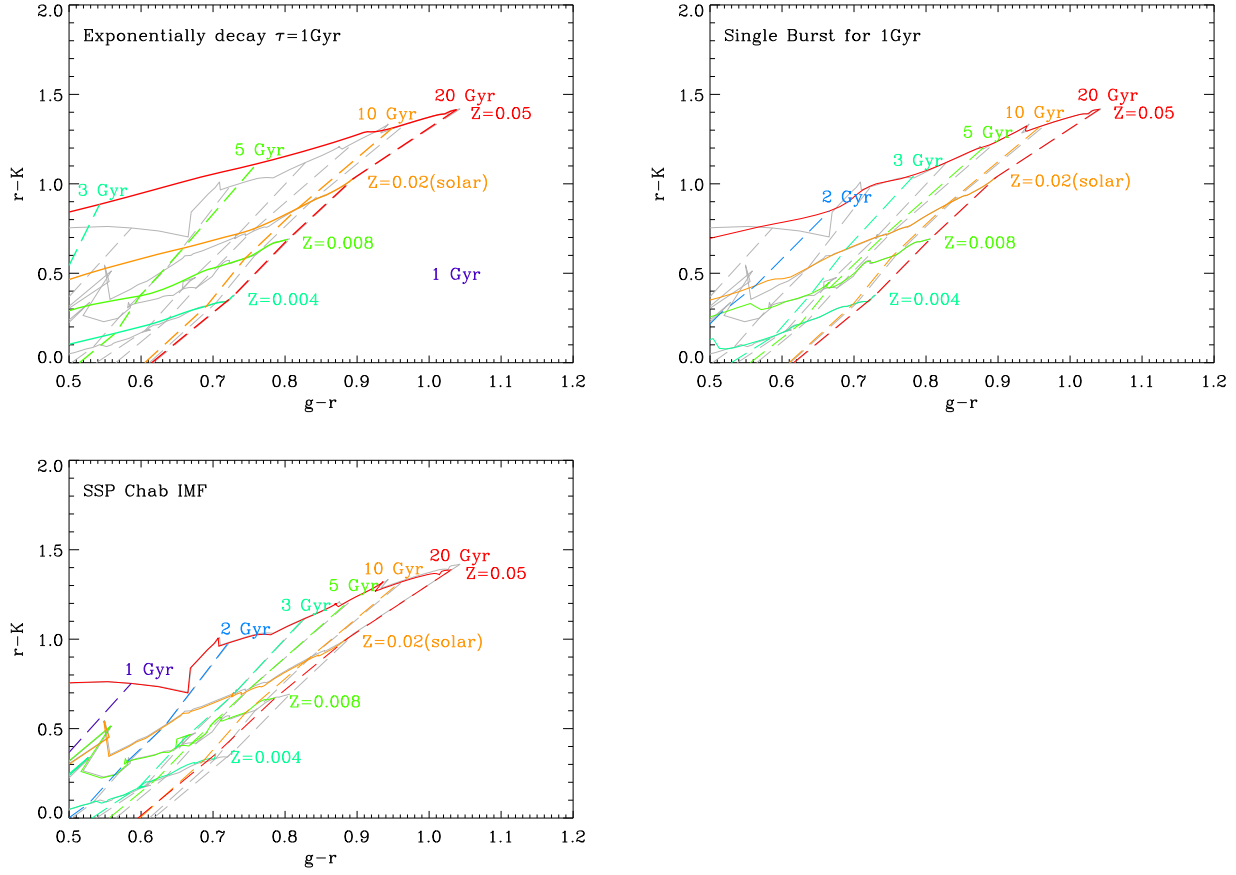


FIG. 14.— Same color color grid as left column of Figure 13 but for BC03 composite stellar population model of exponential decreasing star formation rate ($\tau = 1$ Gyr)(upper left), a single burst expanding 1 Gyr (upper right) and same SSP but with Chabrier IMF (lower right).

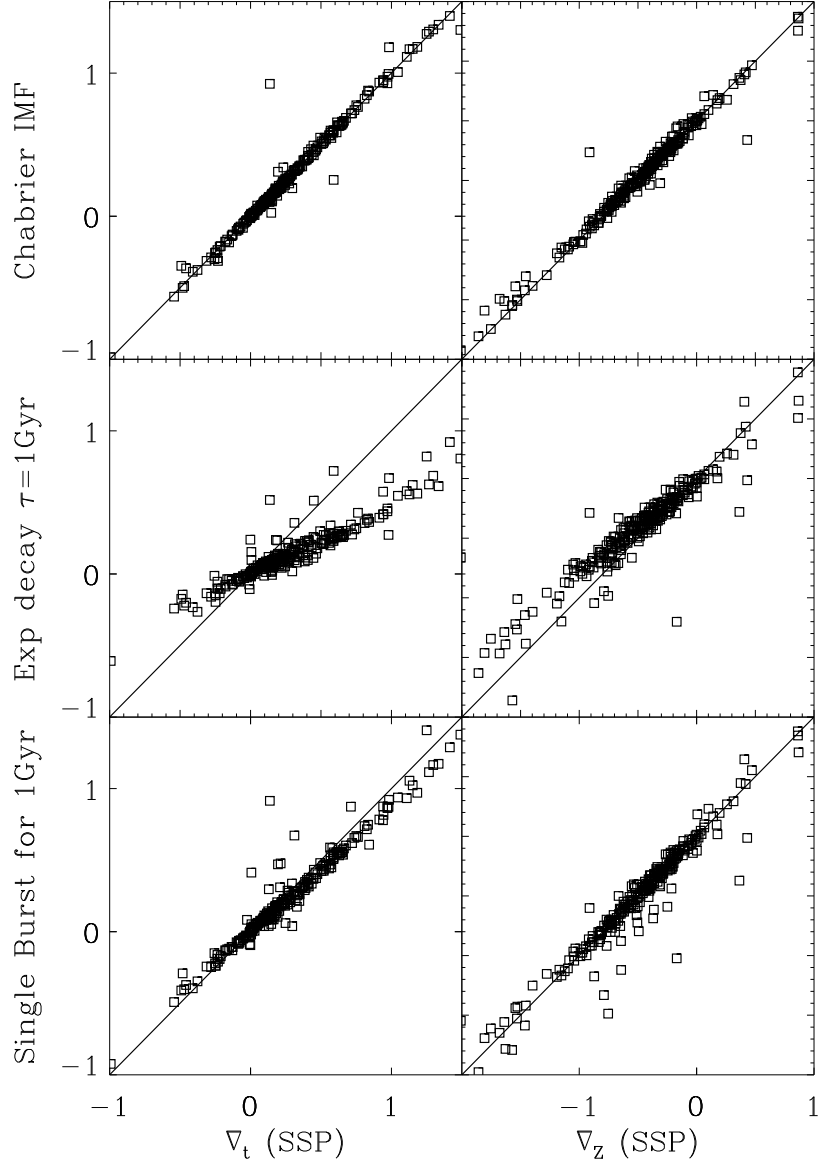


FIG. 15.— Comparison of the gradient values derived by using a different IMF (Chabrier IMF), and different star formation histories (an exponentially decaying SFR with $\tau = 1$ Gyr, and a single burst model with 1 Gyr burst duration). We find that the age gradient become shallower when an extended star formation is added, but the change in the metallicity gradient values is negligible.

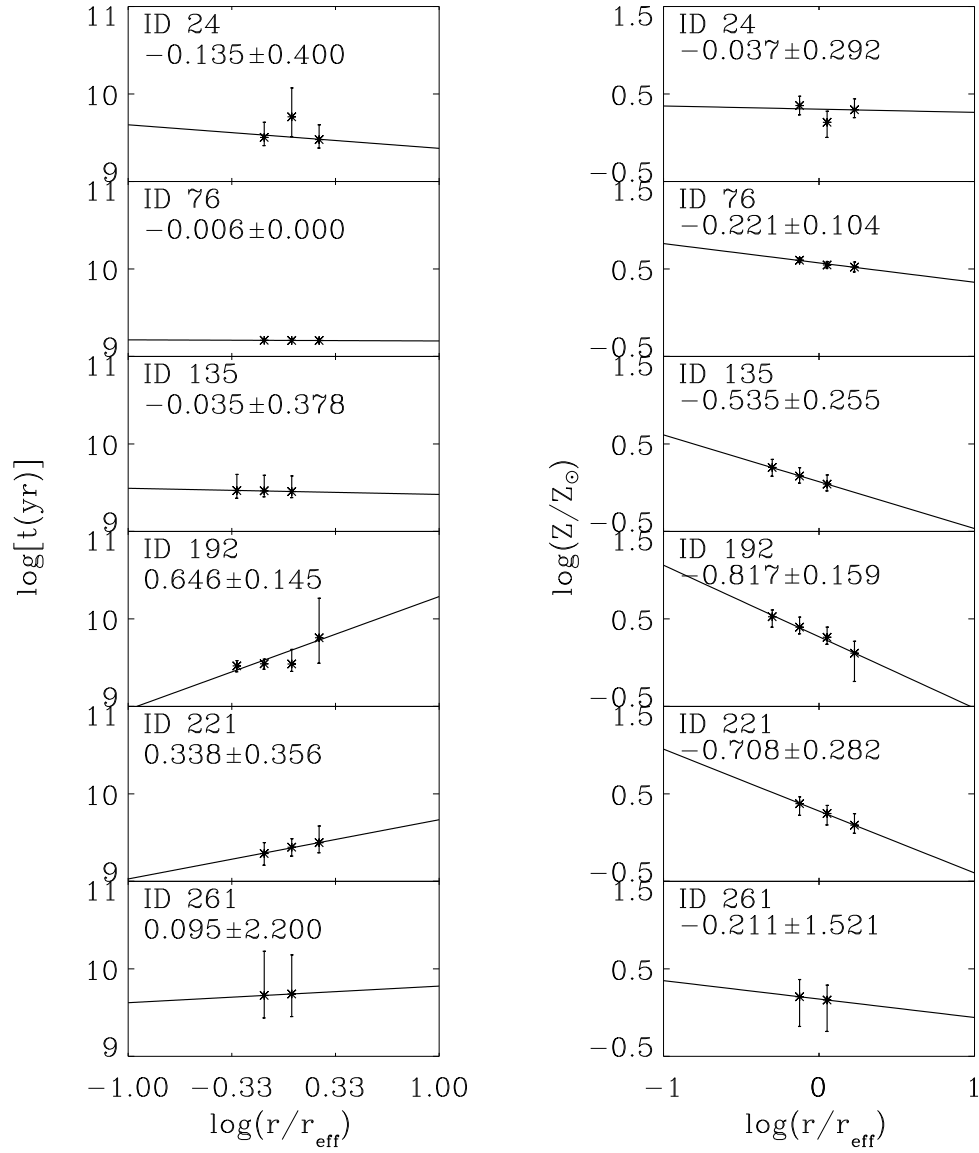


FIG. 16.— Age and the metallicity profiles of elliptical galaxies in the low-mass range ($10^{10.6} M_{\odot} < M_{*} < 10^{10.88} M_{\odot}$). The best-fit lines of the gradients are indicated with solid lines.

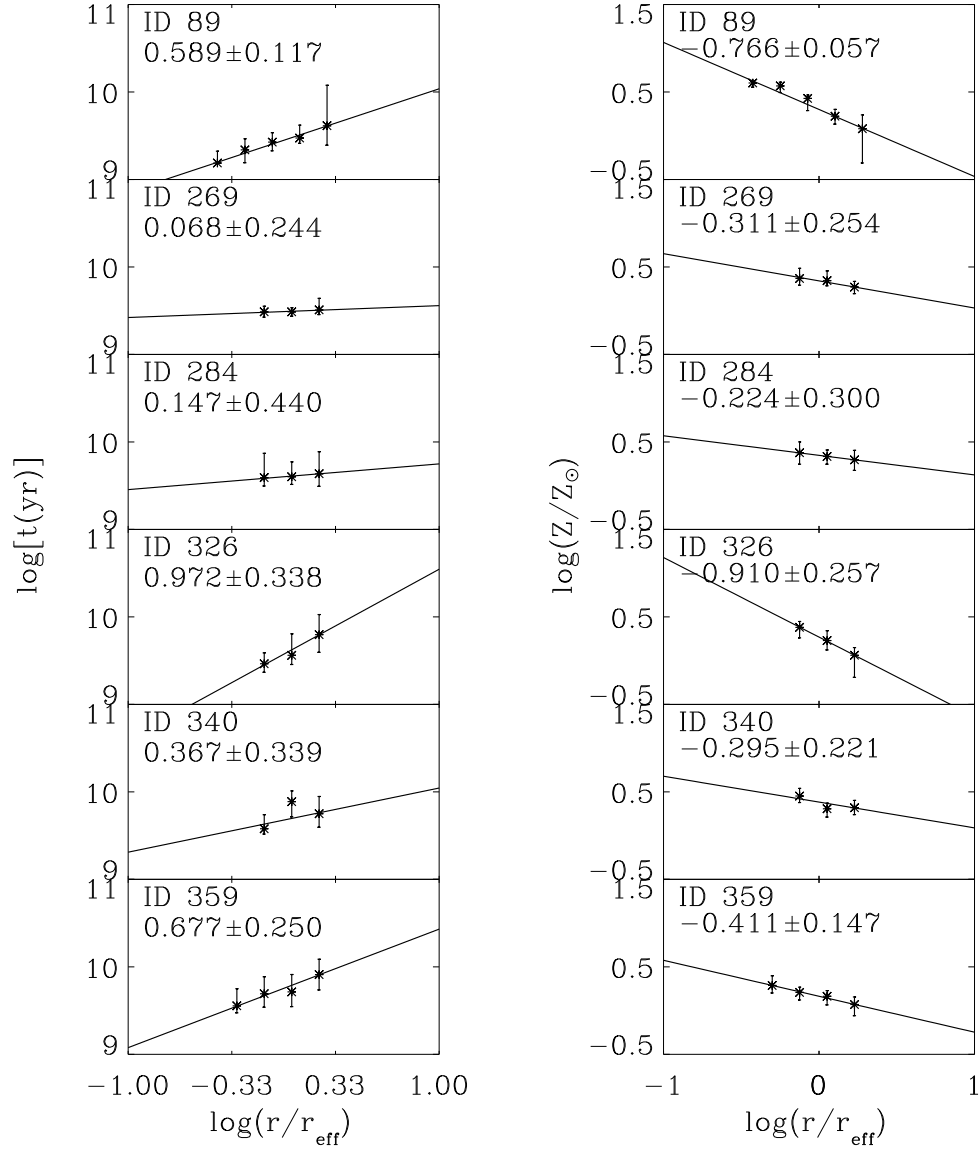


FIG. 17.— Same as Figure 16 but for elliptical galaxies in intermediate mass range ($10^{10.88} M_{\odot} < M_{*} < 10^{11.28} M_{\odot}$).

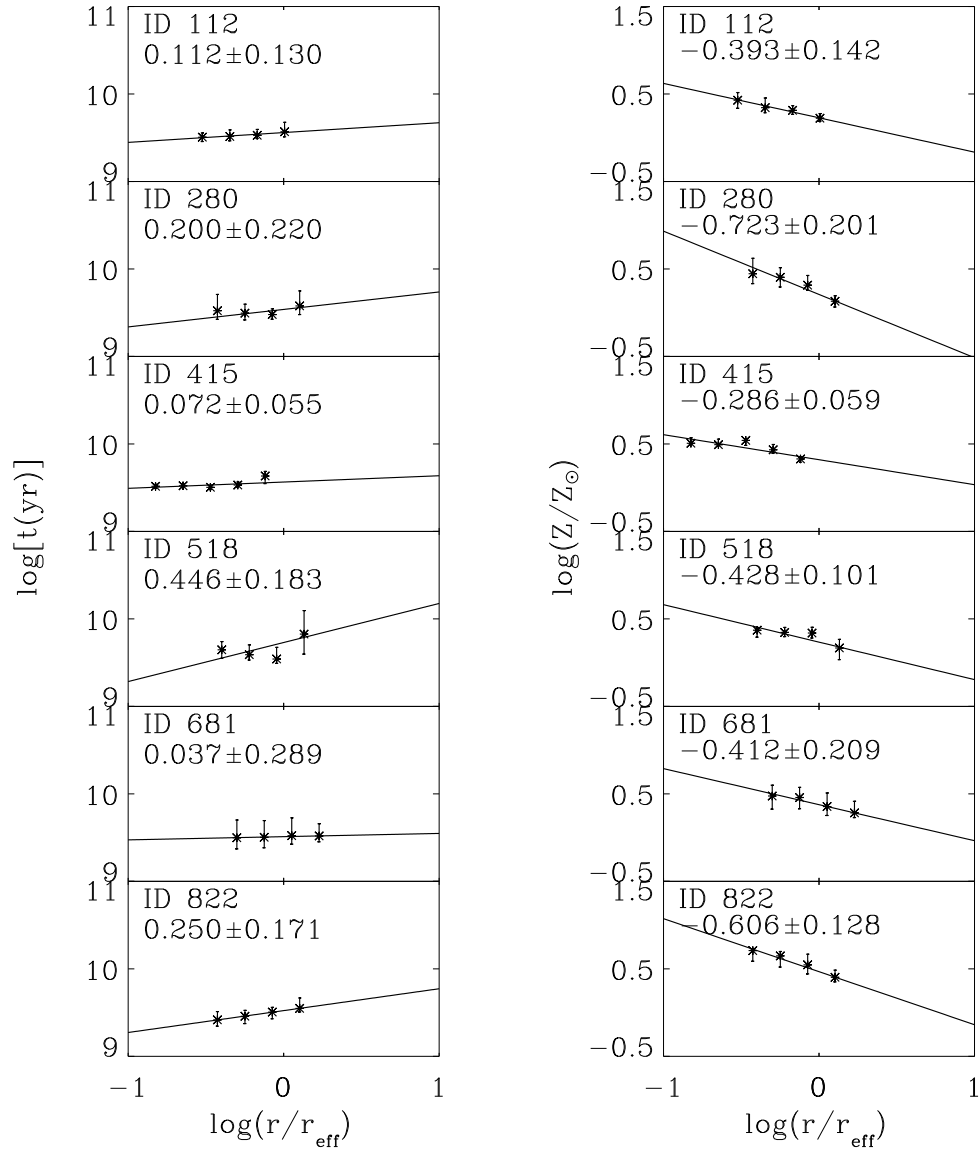


FIG. 18.— Same as Figure 16 but for elliptical galaxies in high-mass range ($M_* > 10^{11.28} M_\odot$).

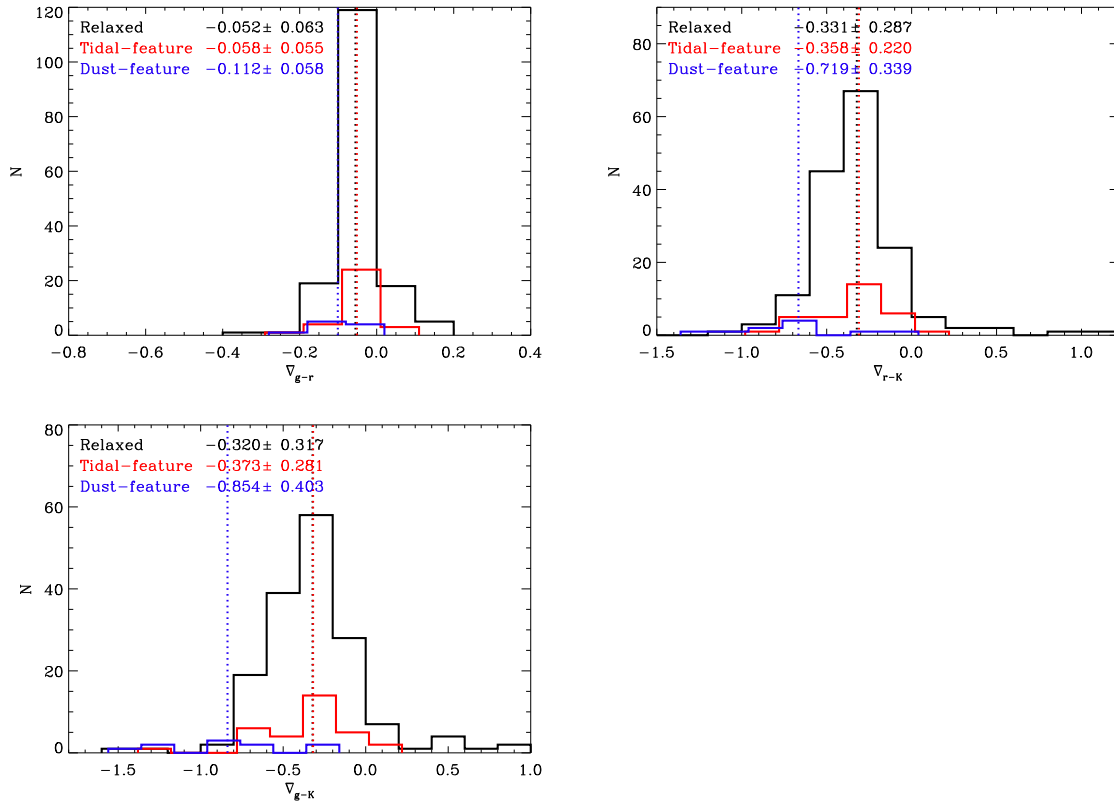


FIG. 19.— The color gradient distributions of each type of elliptical galaxies. The vertical lines indicate median values for each type. We can see that the relaxed types and the tidal-feature types share a similar distributions, but the dust-feature types have steeper gradients than the other two.

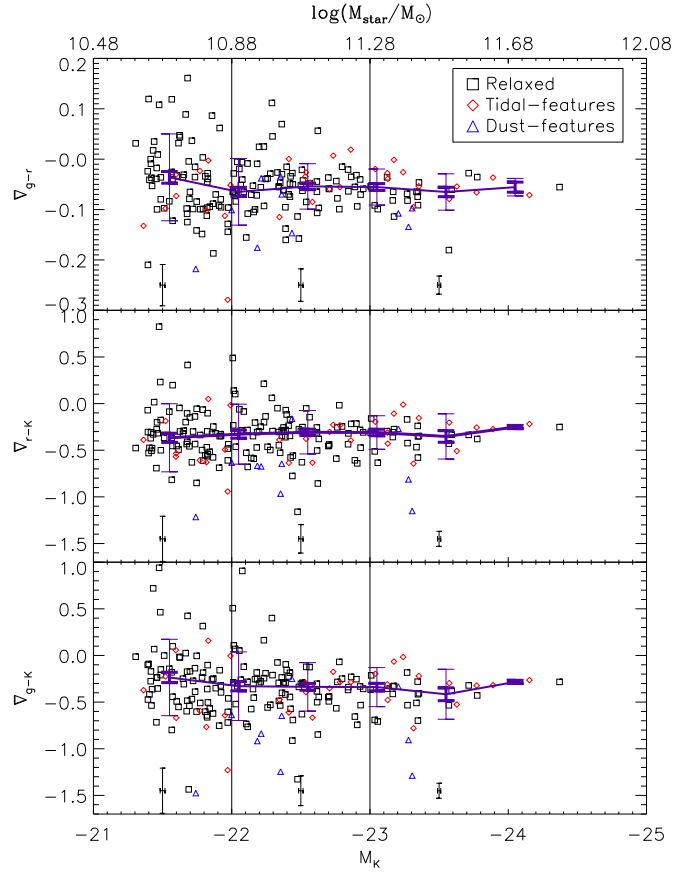


FIG. 20.— The color gradients of the elliptical galaxies as a function of the absolute K -band magnitude (M_K or the stellar mass). The vertical lines are at $M_K = -22$ and -23 which correspond to $10^{10.88}$ and $10^{11.28} M_{\odot}$ in stellar mass. Error bars at the bottom of each panel are median measurement errors of the color gradients of objects in each bin. The thick and the thin error bars along the solid line show the error for the median value and the rms scatter of the color gradients in each mass bin. The figure suggests that the color gradients are nearly constant but their scatter decreases at the highest mass bin over the explored mass range.

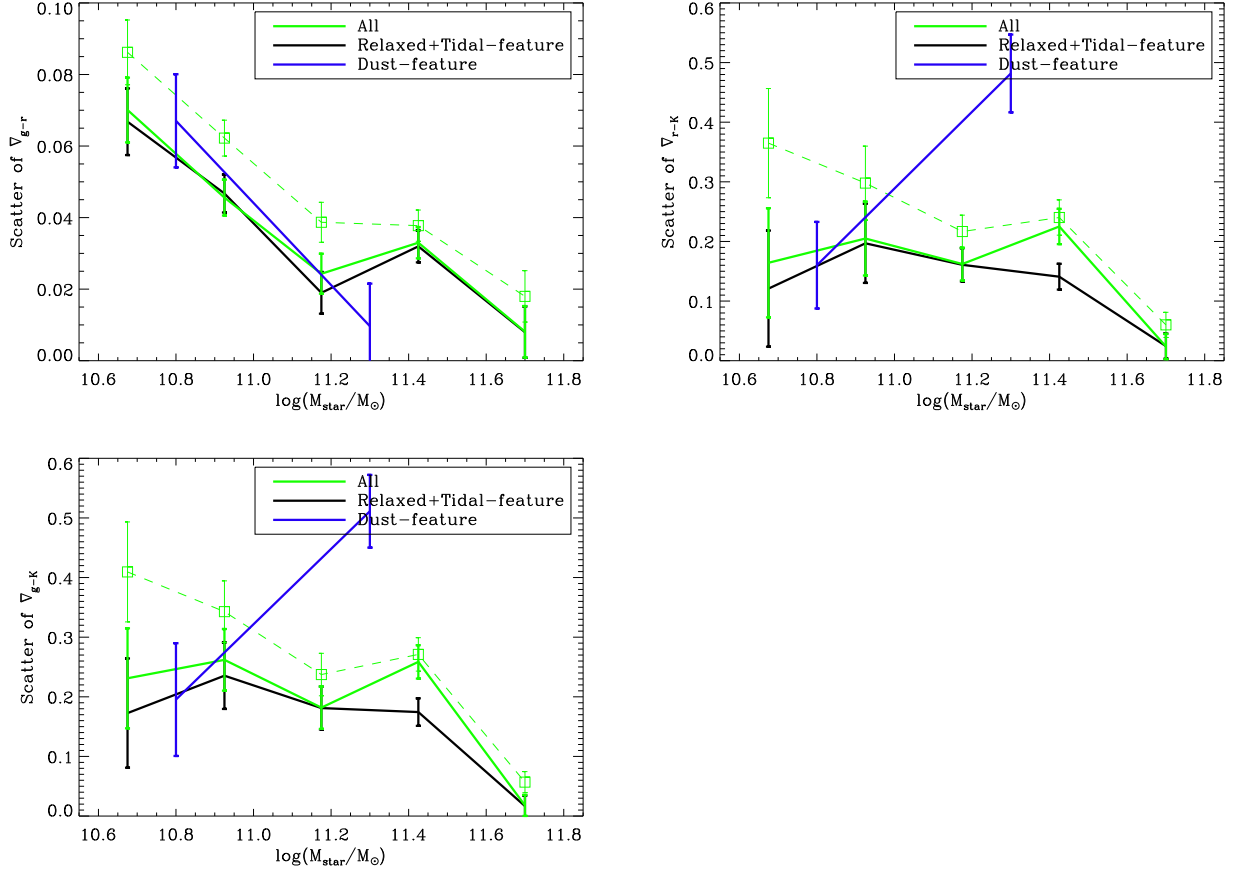


FIG. 21.— The intrinsic scatter of color gradients of ellipticals as a function of stellar mass (solid lines). The dashed green line indicates the scatter as observed, before correcting for the measurement errors. The relaxed and the tidal-feature types show a reduced scatter at the highest mass bin.

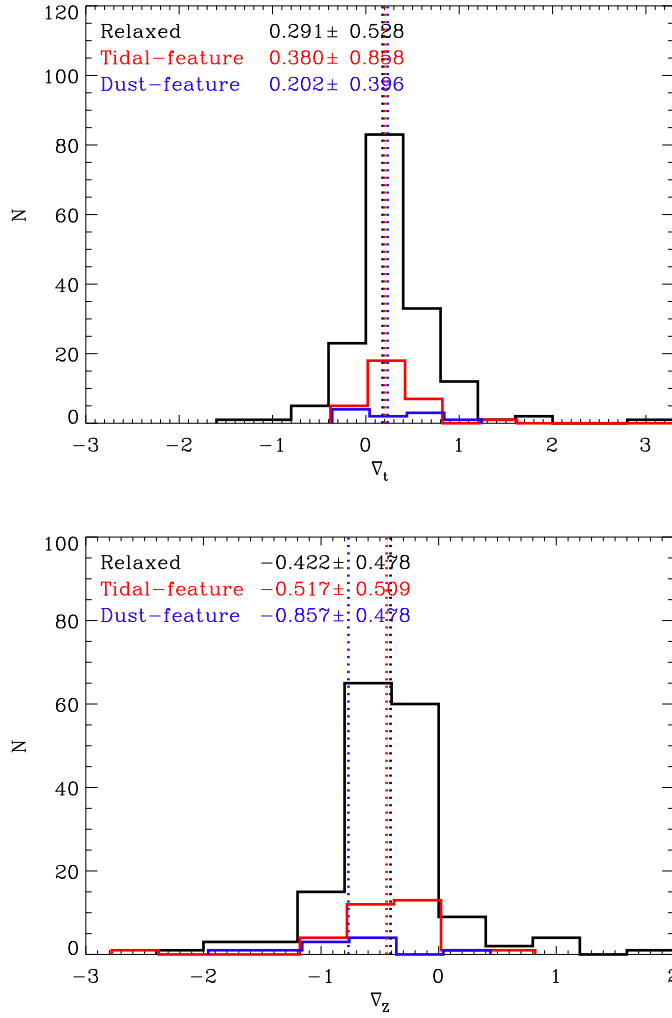


FIG. 22.— The age (top) and the metallicity (bottom) gradient histograms of elliptical galaxies. The vertical lines indicate median values for each type. We can see that the relaxed types and the tidal-feature types share a similar distribution, but the dust-feature types have steeper gradients than the other two, similar to the result we find for the color gradients.

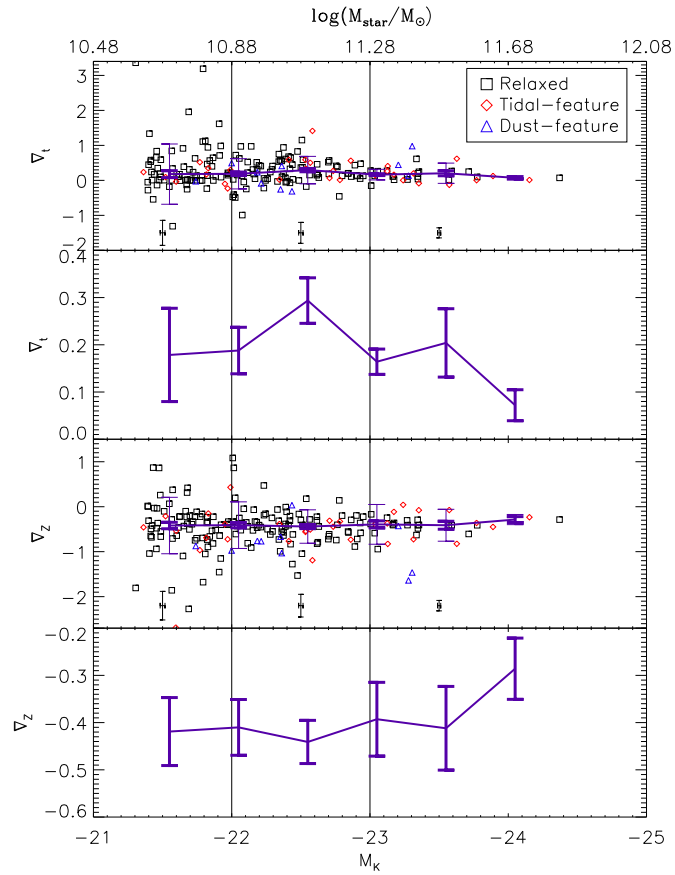


FIG. 23.— Same as Figure 20 but for the age and the metallicity gradients. We also show expanded views of how the median values of the age and the metallicity gradient change as a function of M_K or stellar mass. Both the age and the metallicity gradients appear to show steepening up to $10^{11.4} M_\odot$ but seem to flatten again at the highest mass range.

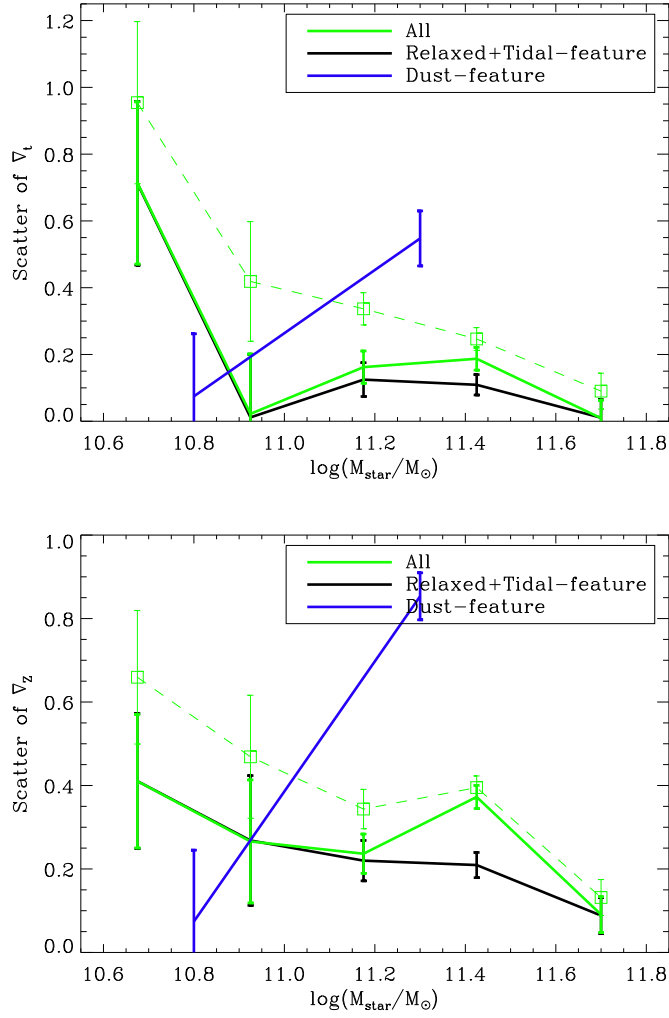


FIG. 24.— Same as Figure 21 but for the age and the metallicity gradients. Like the intrinsic scatters of the color gradients, the relaxed and the tidal-feature types show a reduced scatter at higher mass which can be interpreted as a consequence due major dry merging.

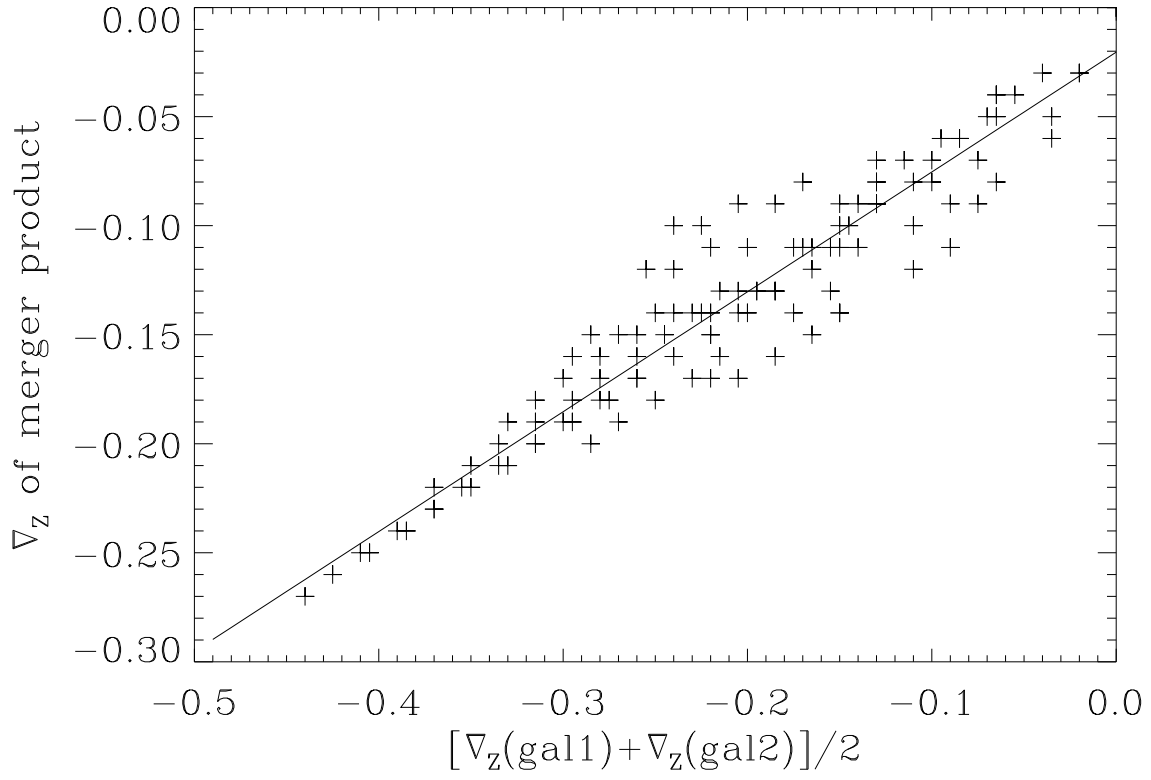


FIG. 25.— The correlation between the average of the input ∇_Z 's of two pre-mergers and the final ∇_Z of the merger product. The data points are taken from a simulation by Di Matteo et al. (2010).

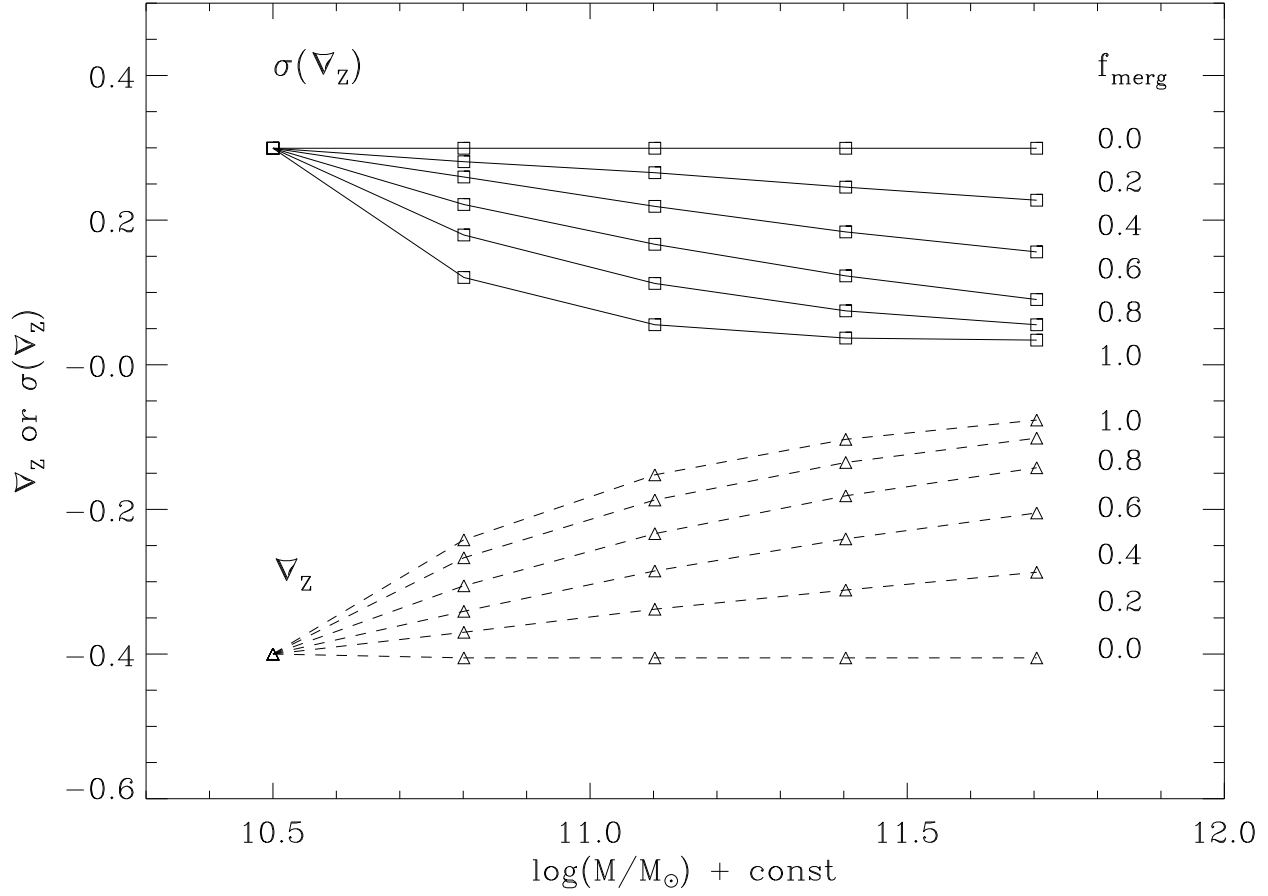


FIG. 26.— This figure shows how the mean metallicity gradient $\langle \nabla_Z \rangle$ and its scatter σ_{∇_Z} changes due to major dry merging, as a function of galaxy mass. The fraction, f_{merg} indicates the fraction of objects that underwent major dry merging. The solid line indicates the change in σ_{∇_Z} , while the dashed line show how $\langle \nabla_Z \rangle$ evolves as a result of the dry merging. Major dry merging reduces the scatter and the mean metallicity gradient value.

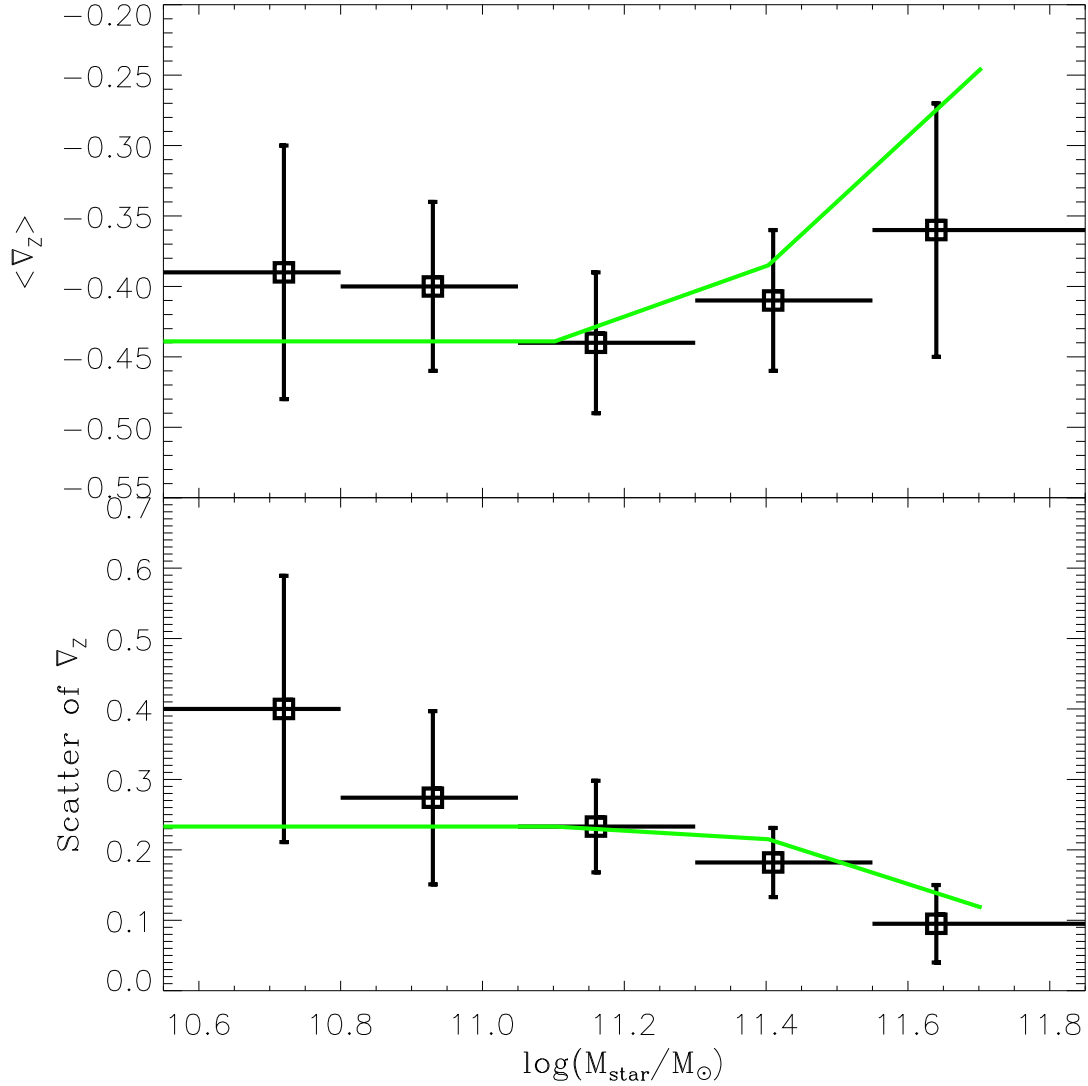


FIG. 27.— The comparison of a simple dry merger model prediction (the green solid line) against the observed median ∇_Z (the points in the upper panel) and the intrinsic σ_{∇_Z} (the points in the lower panel) as a function of the stellar mass. The model lines are for the case where 30% and 90% of ellipticals were assumed to be created via dry merger at the two most massive bins (11.4 and 11.6, correspondingly). Note that a possible flattening of the metallicity gradient and the decrease in its scatter in the observed data, which can be explained by a significant amount of dry merging at $M_{star} > 11.4 M_{\odot}$.

TABLE 1
NUMBER OF ELLIPTICALS IN EACH TYPE

Types	Relaxed	Tidal-feature	Dust-feature	Total
Number	162	32	10	204

TABLE 2
MEDIAN GRADIENTS

Type	∇_{g-r}	∇_{r-K}	∇_{g-K}	∇_t	∇_Z
Relaxed	-0.055 ± 0.005	-0.323 ± 0.022	-0.322 ± 0.025	0.180 ± 0.041	-0.409 ± 0.037
Tidal-feature	-0.051 ± 0.010	-0.310 ± 0.039	-0.319 ± 0.050	0.200 ± 0.152	-0.443 ± 0.090
Dust-feature	-0.101 ± 0.018	-0.666 ± 0.107	-0.837 ± 0.127	0.233 ± 0.125	-0.767 ± 0.151
Total	-0.055 ± 0.004	-0.330 ± 0.020	-0.329 ± 0.023	0.180 ± 0.041	-0.412 ± 0.034

TABLE 3
K-S TEST BETWEEN GRADIENTS OF DIFFERENT TYPES OF ELLIPTICALS

Types	∇_{g-r}	∇_{r-K}	∇_{g-K}	∇_t	∇_Z
Relaxed vs. Tidal-feature	0.951	0.943	0.916	0.953	0.809
Relaxed vs. Dust-feature	0.008	2.8×10^{-5}	1.0×10^{-4}	0.488	0.001

TABLE 4
INTRINSIC SCATTERS OF COLOR/AGE/METALLICITY GRADIENTS

Gradient	Type	$M_K < -23$	$-22 > M_K > -23$	$M_K > -22$
$\sigma_{\nabla_{g-r}}$	All	0.029 ± 0.004	0.069 ± 0.007	0.031 ± 0.004
	Relaxed	0.027 ± 0.004	0.066 ± 0.008	0.030 ± 0.005
	Tidal-feature	0.020 ± 0.007	0.061 ± 0.017	0.022 ± 0.012
	Relaxed & Tidal-feature	0.027 ± 0.004	0.067 ± 0.007	0.029 ± 0.005
$\sigma_{\nabla_{r-K}}$	Dust-feature	0.035 ± 0.013	0.062 ± 0.012	
	All	0.197 ± 0.025	0.125 ± 0.073	0.218 ± 0.052
	Relaxed	0.089 ± 0.024	0.120 ± 0.086	0.223 ± 0.059
	Tidal-feature	0.158 ± 0.027	0.025 ± 0.105	0.060 ± 0.035
$\sigma_{\nabla_{g-K}}$	Relaxed & Tidal-feature	0.122 ± 0.018	0.098 ± 0.077	0.207 ± 0.055
	Dust-feature	0.367 ± 0.067	0.150 ± 0.089	
	All	0.231 ± 0.023	0.242 ± 0.066	0.246 ± 0.045
	Relaxed	0.127 ± 0.026	0.201 ± 0.080	0.234 ± 0.052
σ_{∇_t}	Tidal-feature	0.189 ± 0.029	0.280 ± 0.124	0.072 ± 0.041
	Relaxed & Tidal-feature	0.157 ± 0.020	0.198 ± 0.070	0.223 ± 0.048
	Dust-feature	0.417 ± 0.063	0.218 ± 0.096	
	All	0.144 ± 0.032	0.521 ± 0.200	0.031 ± 0.133
σ_{∇_Z}	Relaxed	0.004 ± 0.048	0.390 ± 0.211	0.023 ± 0.161
	Tidal-feature	0.165 ± 0.039	1.289 ± 0.546	0.248 ± 0.079
	Relaxed & Tidal-feature	0.058 ± 0.032	0.551 ± 0.202	0.042 ± 0.142
	Dust-feature	0.342 ± 0.079	0.090 ± 0.131	
σ_{∇_Z}	All	0.316 ± 0.024	0.323 ± 0.129	0.300 ± 0.123
	Relaxed	0.082 ± 0.032	0.270 ± 0.136	0.304 ± 0.139
	Tidal-feature	0.278 ± 0.042	0.620 ± 0.372	0.109 ± 0.055
	Relaxed & Tidal-feature	0.177 ± 0.026	0.321 ± 0.131	0.307 ± 0.129
Dust-feature	0.586 ± 0.051	0.166 ± 0.090		

TABLE 5
LIST OF ELLIPTICALS AND THEIR PROPERTIES

KID ^a	redshift	$r_{eff,r}$ ^b	$r_{eff,K}$ ^c	∇_{g-r} ^d	∇_{r-K} ^e	∇_{g-K} ^f	∇_t ^g	∇_Z ^h	M_K ⁱ	M_* ^j	B/T ^k	Type ^l
24	0.0350	5.28	3.21	-0.10 ± 0.04	-0.20 ± 0.15	-0.24 ± 0.16	-0.13 ± 0.40	-0.04 ± 0.29	-21.46 ± 0.02	10.66 ± 0.01	1.00	R
76	0.0431	2.35	3.21	-0.10 ± 0.04	-0.34 ± 0.22	-0.51 ± 0.22	-0.01 ± 0.00	-0.22 ± 0.10	-21.77 ± 0.02	10.79 ± 0.01	0.93	R
89	0.0275	7.92	6.42	0.00 ± 0.04	-0.64 ± 0.06	-0.61 ± 0.07	0.59 ± 0.12	-0.77 ± 0.06	-22.41 ± 0.01	11.05 ± 0.00	0.65	T
112	0.0313	11.88	8.03	-0.08 ± 0.01	-0.36 ± 0.08	-0.41 ± 0.08	0.11 ± 0.13	-0.39 ± 0.14	-23.17 ± 0.01	11.35 ± 0.00	0.73	R
135	0.0302	7.92	4.82	-0.07 ± 0.03	-0.53 ± 0.14	-0.67 ± 0.14	-0.04 ± 0.38	-0.54 ± 0.25	-21.60 ± 0.02	10.72 ± 0.01	0.52	T
192	0.0267	5.28	4.82	-0.09 ± 0.02	-0.58 ± 0.12	-0.62 ± 0.12	0.65 ± 0.14	-0.82 ± 0.16	-21.86 ± 0.01	10.83 ± 0.01	0.52	R
221	0.0306	5.28	3.21	-0.04 ± 0.04	-0.45 ± 0.19	-0.44 ± 0.19	0.34 ± 0.36	-0.71 ± 0.28	-21.57 ± 0.02	10.71 ± 0.01	0.79	R
261	0.0422	5.28	3.21	-0.10 ± 0.03	-0.19 ± 0.50	-0.23 ± 0.50	0.09 ± 2.20	-0.21 ± 1.52	-21.52 ± 0.03	10.69 ± 0.01	0.68	T
269	0.0444	5.28	3.21	-0.06 ± 0.02	-0.30 ± 0.13	-0.35 ± 0.14	0.07 ± 0.24	-0.31 ± 0.25	-22.71 ± 0.01	11.16 ± 0.01	0.77	T
272	0.0443	3.52	3.21	0.06 ± 0.04	-0.35 ± 0.32	-0.16 ± 0.33	0.71 ± 0.48	-0.64 ± 0.30	-21.91 ± 0.02	10.85 ± 0.01	0.67	R
280	0.0448	11.88	6.42	-0.09 ± 0.02	-0.64 ± 0.10	-0.78 ± 0.10	0.20 ± 0.22	-0.72 ± 0.20	-23.31 ± 0.01	11.41 ± 0.00	0.52	T
284	0.0500	3.52	3.21	-0.06 ± 0.03	-0.31 ± 0.19	-0.38 ± 0.19	0.15 ± 0.44	-0.22 ± 0.30	-22.62 ± 0.02	11.13 ± 0.01	1.00	R
326	0.0395	5.28	3.21	-0.07 ± 0.04	-0.58 ± 0.14	-0.57 ± 0.15	0.97 ± 0.34	-0.91 ± 0.26	-22.14 ± 0.02	10.94 ± 0.01	0.58	R
340	0.0483	5.28	3.21	-0.05 ± 0.03	-0.29 ± 0.16	-0.30 ± 0.16	0.37 ± 0.34	-0.30 ± 0.22	-22.50 ± 0.02	11.08 ± 0.01	0.57	R
346	0.0497	2.81	3.21	-0.08 ± 0.14	-0.09 ± 0.53	-0.14 ± 0.52	-0.18 ± 1.28	0.07 ± 0.85	-21.55 ± 0.02	10.70 ± 0.01	0.80	R
354	0.0380	1.68	1.61	-0.03 ± 0.09	-0.57 ± 0.75	0.06 ± 0.78	4.76 ± 1.92	-2.69 ± 1.41	-21.60 ± 0.02	10.72 ± 0.01	0.58	T
359	0.0334	7.92	4.82	-0.07 ± 0.03	-0.24 ± 0.07	-0.22 ± 0.08	0.68 ± 0.25	-0.41 ± 0.15	-22.41 ± 0.01	11.04 ± 0.01	0.52	R
415	0.0453	17.82	16.05	-0.06 ± 0.01	-0.25 ± 0.03	-0.28 ± 0.03	0.07 ± 0.05	-0.29 ± 0.06	-24.37 ± 0.02	11.83 ± 0.01	0.82	R
448	0.0274	7.92	4.82	-0.01 ± 0.01	-0.31 ± 0.08	-0.33 ± 0.08	0.15 ± 0.12	-0.43 ± 0.09	-22.04 ± 0.01	10.90 ± 0.00	0.69	R
477	0.0475	4.22	3.21	-0.14 ± 0.07	-0.85 ± 0.64	-0.60 ± 0.65	0.00 ± 0.00	-0.70 ± 0.35	-21.75 ± 0.02	10.78 ± 0.01	0.53	R
481	0.0177	17.82	14.45	-0.11 ± 0.01	-0.49 ± 0.06	-0.64 ± 0.06	-0.10 ± 0.22	-0.39 ± 0.13	-21.95 ± 0.02	10.86 ± 0.01	0.68	T
483	0.0353	3.52	3.21	-0.07 ± 0.06	-0.15 ± 0.19	-0.17 ± 0.19	0.00 ± 0.00	-0.20 ± 0.34	-21.70 ± 0.01	10.76 ± 0.00	0.56	R
506	0.0476	7.92	4.82	-0.10 ± 0.03	-0.02 ± 0.14	-0.07 ± 0.13	-0.46 ± 0.63	0.14 ± 0.29	-22.78 ± 0.02	11.19 ± 0.01	0.56	R
518	0.0407	7.92	6.02	-0.11 ± 0.01	-0.27 ± 0.07	-0.33 ± 0.07	0.45 ± 0.18	-0.43 ± 0.10	-23.21 ± 0.01	11.36 ± 0.00	0.71	D
528	0.0412	11.88	4.41	-0.04 ± 0.03	-0.67 ± 0.16	-0.84 ± 0.14	-0.09 ± 0.29	-0.77 ± 0.23	-22.21 ± 0.02	10.97 ± 0.01	0.50	D
536	0.0387	5.28	4.82	-0.10 ± 0.07	-0.63 ± 0.37	-0.64 ± 0.38	0.49 ± 0.62	-0.97 ± 0.59	-22.00 ± 0.02	10.88 ± 0.01	0.58	D
537	0.0369	7.92	4.82	-0.09 ± 0.02	-0.20 ± 0.11	-0.24 ± 0.11	0.06 ± 0.43	-0.19 ± 0.18	-22.23 ± 0.02	10.97 ± 0.01	0.56	R
556	0.0326	5.28	3.21	0.02 ± 0.03	-0.30 ± 0.13	-0.30 ± 0.13	0.43 ± 0.26	-0.41 ± 0.19	-22.20 ± 0.02	10.96 ± 0.01	0.87	R
560	0.0235	5.28	4.82	-0.21 ± 0.04	-0.30 ± 0.12	-0.47 ± 0.12	-0.28 ± 0.22	0.00 ± 0.16	-21.39 ± 0.01	10.64 ± 0.00	0.62	R
561	0.0494	3.52	3.21	0.01 ± 0.06	-0.23 ± 0.19	-0.18 ± 0.21	0.27 ± 0.54	-0.44 ± 0.40	-22.73 ± 0.02	11.17 ± 0.01	0.75	T
597	0.0460	3.52	3.21	-0.01 ± 0.05	-0.29 ± 0.24	-0.30 ± 0.25	0.13 ± 0.32	-0.36 ± 0.16	-22.07 ± 0.02	10.91 ± 0.01	0.59	R
601	0.0474	5.28	3.21	0.05 ± 0.05	-0.29 ± 0.20	-0.21 ± 0.21	0.41 ± 0.41	-0.55 ± 0.29	-22.30 ± 0.03	11.00 ± 0.01	0.74	R
606	0.0468	5.28	4.82	-0.06 ± 0.03	-0.61 ± 0.12	-0.66 ± 0.12	0.43 ± 0.18	-0.89 ± 0.17	-22.89 ± 0.01	11.24 ± 0.00	0.73	R
624	0.0426	3.52	3.21	-0.08 ± 0.07	-0.33 ± 0.29	-0.32 ± 0.28	0.98 ± 1.20	-1.15 ± 0.72	-21.92 ± 0.02	10.85 ± 0.01	0.64	R
639	0.0337	5.28	3.21	-0.04 ± 0.05	-0.47 ± 0.25	-0.42 ± 0.26	1.34 ± 0.47	-1.04 ± 0.35	-21.40 ± 0.02	10.64 ± 0.01	0.70	R
640	0.0418	5.50	8.03	-0.07 ± 0.03	-0.47 ± 0.12	-0.18 ± 0.39	0.52 ± 1.73	-0.34 ± 1.16	-22.18 ± 0.05	10.95 ± 0.02	0.64	R
675	0.0366	5.28	4.82	-0.06 ± 0.03	-0.45 ± 0.10	-0.49 ± 0.10	0.75 ± 0.19	-0.73 ± 0.14	-22.34 ± 0.02	11.02 ± 0.01	0.74	R
681	0.0427	7.92	4.82	-0.09 ± 0.03	-0.35 ± 0.10	-0.42 ± 0.10	0.04 ± 0.29	-0.41 ± 0.21	-23.35 ± 0.01	11.42 ± 0.00	0.94	R
723	0.0473	3.52	3.21	-0.05 ± 0.06	-0.33 ± 0.14	-0.33 ± 0.14	0.50 ± 0.43	-0.51 ± 0.31	-22.57 ± 0.02	11.11 ± 0.01	0.87	T
731	0.0456	2.99	3.21	0.12 ± 0.08	-0.53 ± 0.41	-0.09 ± 0.40	0.45 ± 0.81	-0.31 ± 0.54	-21.40 ± 0.03	10.64 ± 0.01	0.71	R
739	0.0297	7.92	4.82	-0.04 ± 0.10	1.03 ± 0.88	0.91 ± 0.84	-0.99 ± 3.21	1.64 ± 2.27	-22.08 ± 0.02	10.91 ± 0.01	0.64	R
745	0.0475	5.28	4.82	-0.11 ± 0.03	-0.50 ± 0.15	-0.50 ± 0.16	0.46 ± 0.39	-0.82 ± 0.29	-22.62 ± 0.02	11.13 ± 0.01	0.77	R
776	0.0467	4.24	3.21	-0.10 ± 0.04	-0.59 ± 0.34	-0.45 ± 0.34	0.18 ± 0.53	-0.07 ± 0.42	-22.16 ± 0.03	10.94 ± 0.01	1.00	R
789	0.0405	5.28	4.82	-0.04 ± 0.02	-0.28 ± 0.11	-0.33 ± 0.11	0.05 ± 0.22	-0.36 ± 0.20	-22.93 ± 0.01	11.25 ± 0.01	0.78	R
822	0.0479	11.88	6.42	-0.03 ± 0.03	-0.34 ± 0.08	-0.32 ± 0.08	0.25 ± 0.17	-0.61 ± 0.13	-23.71 ± 0.01	11.57 ± 0.00	0.71	R
825	0.0236	17.82	6.02	-0.15 ± 0.03	-0.16 ± 0.08	-0.25 ± 0.08	-0.31 ± 0.18	0.03 ± 0.13	-22.44 ± 0.01	11.05 ± 0.00	0.55	D
829	0.0485	11.88	6.42	-0.05 ± 0.02	-0.51 ± 0.10	-0.53 ± 0.10	0.62 ± 0.17	-0.82 ± 0.18	-23.63 ± 0.01	11.53 ± 0.00	0.57	T
831	0.0490	6.50	4.82	-0.06 ± 0.01	-0.31 ± 0.06	-0.36 ± 0.06	0.13 ± 0.15	-0.22 ± 0.08	-22.95 ± 0.01	11.26 ± 0.00	0.72	R
844	0.0346	5.28	4.82	-0.08 ± 0.02	-0.05 ± 0.11	-0.12 ± 0.11	-0.18 ± 0.23	0.18 ± 0.22	-22.54 ± 0.02	11.10 ± 0.01	0.90	R
900	0.0440	5.28	3.21	0.02 ± 0.04	-0.40 ± 0.22	-0.29 ± 0.22	0.56 ± 0.30	-0.73 ± 0.25	-22.86 ± 0.02	11.22 ± 0.01	0.66	T
947	0.0443	5.28	3.21	-0.10 ± 0.03	-0.38 ± 0.10	-0.45 ± 0.10	0.08 ± 0.26	-0.44 ± 0.21	-22.63 ± 0.01	11.13 ± 0.00	0.69	R
983	0.0127	11.88	14.45	-0.06 ± 0.02	-0.25 ± 0.03	-0.28 ± 0.03	0.41 ± 0.09	-0.45 ± 0.05	-22.21 ± 0.01	10.96 ± 0.00	0.96	R
1006	0.0500	2.88	3.21	-0.09 ± 0.06	-0.69 ± 0.67	-0.75 ± 0.68	1.62 ± 2.17	-1.46 ± 1.25	-21.91 ± 0.02	10.84 ± 0.01	0.95	R
1025	0.0480	2.35	1.61	0.11 ± 0.15	0.82 ± 1.06	0.94 ± 1.07	0.00 ± 0.00	0.86 ± 0.98	-21.47 ± 0.02	10.67 ± 0.01	0.51	R
1029	0.0498	3.58	3.21	-0.02 ± 0.10	-0.44 ± 0.23	-0.37 ± 0.41	0.19 ± 0.98	-0.55 ± 0.60	-22.84 ± 0.01	11.22 ± 0.00	0.84	R
1098	0.0472	3.01	3.21	0.04 ± 0.06	-0.30 ± 0.53	-0.02 ± 0.53	-0.01 ± 0.00	-0.21 ± 0.95	-21.63 ± 0.04	10.73 ± 0.02	0.81	R

Color Gradients of Elliptical Galaxies

TABLE 5 — *Continued*

KID ^a	redshift	$r_{eff,r}$ ^b	$r_{eff,K}$ ^c	∇_{g-r} ^d	∇_{r-K} ^e	∇_{g-K} ^f	∇_t ^g	∇_Z ^h	M_K ⁱ	M_* ^j	B/T ^k	Type ^l
1103	0.0392	7.92	3.21	-0.10 ± 0.14	-0.20 ± 0.65	-0.25 ± 0.69	0.05 ± 2.87	-0.33 ± 1.73	-22.17 ± 0.01	10.95 ± 0.01	0.96	R
1108	0.0468	4.18	3.21	0.09 ± 0.03	-0.20 ± 0.60	0.03 ± 0.61	0.01 ± 0.00	-0.10 ± 0.84	-21.67 ± 0.02	10.75 ± 0.01	0.63	R
1114	0.0440	5.28	4.82	-0.03 ± 0.04	-0.58 ± 0.21	-0.57 ± 0.21	0.65 ± 0.29	-0.83 ± 0.26	-22.43 ± 0.01	11.05 ± 0.01	0.93	R
1115	0.0446	2.92	3.21	-0.03 ± 0.08	0.14 ± 0.37	0.11 ± 0.37	-0.41 ± 0.82	0.86 ± 0.60	-22.02 ± 0.02	10.89 ± 0.01	0.55	R
1116	0.0443	2.35	3.21	-0.06 ± 0.08	0.49 ± 0.23	0.51 ± 0.23	-0.47 ± 0.72	1.08 ± 0.42	-22.01 ± 0.02	10.88 ± 0.01	0.78	R
1177	0.0441	3.52	4.82	-0.01 ± 0.03	-0.31 ± 0.20	-0.26 ± 0.20	0.32 ± 0.25	-0.47 ± 0.25	-22.18 ± 0.02	10.95 ± 0.01	0.53	R
1186	0.0421	5.28	4.82	-0.11 ± 0.03	-0.68 ± 0.20	-0.76 ± 0.20	0.52 ± 0.19	-0.81 ± 0.24	-22.12 ± 0.03	10.93 ± 0.01	0.95	R
1191	0.0431	3.52	3.21	0.00 ± 0.00	-0.37 ± 0.27	-0.28 ± 0.27	0.53 ± 0.36	-0.65 ± 0.25	-21.41 ± 0.02	10.65 ± 0.01	1.00	R
1203	0.0435	4.18	3.21	-0.10 ± 0.04	-0.37 ± 0.55	-0.00 ± 0.00	0.01 ± 0.00	-0.10 ± 0.29	-21.51 ± 0.03	10.68 ± 0.01	0.73	R
1217	0.0232	11.88	6.02	-0.22 ± 0.04	-1.22 ± 0.08	-1.48 ± 0.08	-0.03 ± 0.13	-0.87 ± 0.04	-21.74 ± 0.01	10.78 ± 0.00	0.61	D
1221	0.0432	3.52	4.82	-0.10 ± 0.05	-0.36 ± 0.20	-0.42 ± 0.21	0.07 ± 0.30	-0.44 ± 0.25	-22.39 ± 0.01	11.04 ± 0.01	0.57	R
1228	0.0214	11.88	8.03	-0.06 ± 0.01	-0.25 ± 0.04	-0.29 ± 0.04	0.37 ± 0.15	-0.40 ± 0.10	-22.51 ± 0.01	11.08 ± 0.00	0.52	R
1238	0.0233	7.92	4.82	0.01 ± 0.03	-0.32 ± 0.09	-0.35 ± 0.09	0.35 ± 0.30	-0.37 ± 0.18	-21.47 ± 0.02	10.67 ± 0.01	0.57	R
1254	0.0495	5.28	3.21	-0.04 ± 0.04	-0.46 ± 0.32	-0.56 ± 0.31	0.05 ± 0.44	-0.50 ± 0.43	-22.26 ± 0.03	10.98 ± 0.01	0.69	R
1280	0.0275	5.28	3.21	-0.09 ± 0.03	-0.52 ± 0.17	-0.57 ± 0.17	0.57 ± 0.39	-0.66 ± 0.29	-21.84 ± 0.01	10.82 ± 0.00	0.85	R
1287	0.0446	5.28	3.21	-0.02 ± 0.04	-0.06 ± 0.15	0.05 ± 0.16	0.63 ± 0.59	-0.25 ± 0.34	-22.06 ± 0.02	10.90 ± 0.01	0.63	R
1322	0.0437	11.88	9.63	-0.06 ± 0.01	-0.47 ± 0.08	-0.51 ± 0.08	0.61 ± 0.13	-0.63 ± 0.12	-23.34 ± 0.02	11.41 ± 0.01	0.59	R
1330	0.0419	3.52	2.81	-0.03 ± 0.03	-0.45 ± 0.48	-0.49 ± 0.48	0.17 ± 0.43	-0.64 ± 0.54	-21.60 ± 0.02	10.72 ± 0.01	0.89	R
1335	0.0454	7.92	4.82	-0.07 ± 0.02	-0.47 ± 0.12	-0.53 ± 0.12	0.47 ± 0.30	-0.58 ± 0.22	-22.93 ± 0.01	11.25 ± 0.01	0.53	R
1339	0.0443	5.28	4.82	-0.05 ± 0.03	-0.30 ± 0.13	-0.29 ± 0.12	0.54 ± 0.38	-0.31 ± 0.28	-22.34 ± 0.02	11.02 ± 0.01	0.99	R
1352	0.0361	5.28	4.82	-0.02 ± 0.03	-0.43 ± 0.20	-0.39 ± 0.19	0.63 ± 0.28	-0.75 ± 0.29	-21.74 ± 0.05	10.77 ± 0.02	0.73	R
1367	0.0359	5.28	3.21	-0.16 ± 0.04	-0.53 ± 0.16	-0.73 ± 0.16	-0.25 ± 0.36	-0.35 ± 0.28	-22.11 ± 0.01	10.92 ± 0.00	0.65	R
1377	0.0421	4.24	3.21	-0.19 ± 0.03	-0.25 ± 0.27	-0.25 ± 0.28	-0.00 ± 0.00	-0.22 ± 0.36	-21.87 ± 0.02	10.83 ± 0.01	0.58	R
1406	0.0493	5.28	6.42	-0.00 ± 0.03	-0.11 ± 0.18	-0.07 ± 0.18	0.16 ± 0.27	-0.11 ± 0.26	-23.17 ± 0.03	11.35 ± 0.01	0.74	T
1421	0.0248	5.28	4.82	-0.01 ± 0.04	-0.31 ± 0.18	-0.17 ± 0.18	0.58 ± 0.21	-0.49 ± 0.15	-21.42 ± 0.01	10.65 ± 0.01	0.64	R
1436	0.0364	7.92	6.42	-0.03 ± 0.03	-0.31 ± 0.09	-0.31 ± 0.09	0.26 ± 0.16	-0.37 ± 0.09	-23.13 ± 0.01	11.33 ± 0.01	0.57	T
1440	0.0489	5.28	3.21	-0.09 ± 0.04	-0.51 ± 0.15	-0.69 ± 0.16	0.13 ± 0.78	-0.59 ± 0.32	-23.03 ± 0.01	11.29 ± 0.01	0.82	R
1451	0.0466	3.52	3.21	-0.08 ± 0.07	-0.06 ± 0.22	-0.00 ± 0.20	0.13 ± 0.36	-0.11 ± 0.32	-21.75 ± 0.01	10.78 ± 0.01	0.53	R
1461	0.0419	5.28	4.82	-0.01 ± 0.04	-0.28 ± 0.22	-0.28 ± 0.23	0.22 ± 0.33	-0.44 ± 0.28	-22.11 ± 0.02	10.93 ± 0.01	0.59	R
1462	0.0451	7.92	4.82	-0.10 ± 0.02	-0.63 ± 0.08	-0.71 ± 0.08	0.26 ± 0.15	-0.94 ± 0.12	-23.06 ± 0.01	11.30 ± 0.00	0.60	R
1470	0.0472	3.94	3.21	0.07 ± 0.02	-0.29 ± 0.12	-0.24 ± 0.12	0.56 ± 0.13	-0.56 ± 0.09	-22.36 ± 0.01	11.02 ± 0.00	0.57	R
1477	0.0443	5.28	4.82	-0.09 ± 0.02	-0.64 ± 0.20	-0.74 ± 0.20	0.13 ± 0.22	-0.72 ± 0.31	-22.91 ± 0.01	11.24 ± 0.00	0.65	R
1526	0.0370	5.18	4.82	0.03 ± 0.03	-0.48 ± 0.35	-0.01 ± 0.37	3.36 ± 1.22	-1.81 ± 0.73	-21.31 ± 0.04	10.60 ± 0.02	0.60	R
1551	0.0439	3.17	3.21	0.03 ± 0.12	-0.49 ± 0.51	-0.55 ± 0.50	0.10 ± 0.51	-0.46 ± 0.48	-21.62 ± 0.03	10.73 ± 0.01	0.65	R
1670	0.0431	5.28	4.82	-0.05 ± 0.06	-0.15 ± 0.11	-0.13 ± 0.12	0.15 ± 0.34	-0.28 ± 0.21	-22.56 ± 0.01	11.11 ± 0.00	0.60	R
1694	0.0370	3.38	3.21	-0.04 ± 0.03	-0.50 ± 0.20	-0.15 ± 0.22	0.59 ± 0.45	-0.55 ± 0.25	-21.49 ± 0.02	10.67 ± 0.01	0.76	R
1698	0.0393	5.28	4.82	-0.04 ± 0.03	-0.22 ± 0.07	-0.23 ± 0.07	0.11 ± 0.22	-0.29 ± 0.14	-22.86 ± 0.03	11.23 ± 0.01	0.61	R
1737	0.0462	5.28	4.82	-0.02 ± 0.03	-0.12 ± 0.16	-0.16 ± 0.16	-0.03 ± 0.32	-0.11 ± 0.24	-22.40 ± 0.02	11.04 ± 0.01	0.64	R
1775	0.0411	3.52	3.21	-0.08 ± 0.03	-0.18 ± 0.20	-0.21 ± 0.20	0.10 ± 0.17	-0.66 ± 0.20	-21.49 ± 0.01	10.67 ± 0.00	1.00	R
1777	0.0407	11.88	6.42	-0.05 ± 0.01	-0.35 ± 0.04	-0.41 ± 0.04	0.25 ± 0.09	-0.41 ± 0.06	-23.35 ± 0.01	11.42 ± 0.01	0.63	R
1779	0.0407	5.28	4.82	-0.04 ± 0.04	-0.26 ± 0.08	-0.30 ± 0.09	0.18 ± 0.21	-0.31 ± 0.13	-22.62 ± 0.01	11.13 ± 0.00	0.69	R
1790	0.0424	4.23	3.21	0.16 ± 0.03	0.41 ± 0.65	0.42 ± 0.65	0.42 ± 0.00	0.42 ± 0.29	-21.68 ± 0.02	10.75 ± 0.01	0.62	R
1791	0.0414	3.52	3.21	-0.00 ± 0.07	0.05 ± 0.23	0.16 ± 0.25	0.35 ± 0.66	-0.15 ± 0.72	-21.83 ± 0.02	10.81 ± 0.01	0.60	T
1792	0.0419	5.28	4.82	-0.08 ± 0.04	-0.46 ± 0.16	-0.52 ± 0.16	0.72 ± 0.55	-0.61 ± 0.34	-22.03 ± 0.03	10.89 ± 0.01	0.73	R
1808	0.0418	7.92	6.42	-0.06 ± 0.02	-0.32 ± 0.11	-0.34 ± 0.11	0.20 ± 0.29	-0.57 ± 0.24	-22.84 ± 0.02	11.22 ± 0.01	0.56	R
1818	0.0450	5.28	2.81	-0.07 ± 0.04	-0.64 ± 0.30	-0.65 ± 0.30	0.41 ± 0.32	-1.03 ± 0.39	-22.36 ± 0.01	11.02 ± 0.00	0.84	D
1823	0.0387	11.88	6.42	-0.04 ± 0.02	-0.27 ± 0.03	-0.32 ± 0.03	0.13 ± 0.11	-0.45 ± 0.09	-23.89 ± 0.01	11.64 ± 0.00	0.69	T
1862	0.0224	5.28	3.21	-0.02 ± 0.02	-0.07 ± 0.13	-0.10 ± 0.13	-0.05 ± 0.27	0.02 ± 0.21	-21.39 ± 0.01	10.64 ± 0.00	0.51	R
1864	0.0473	2.74	3.21	-0.03 ± 0.08	-0.55 ± 0.32	-0.60 ± 0.32	1.13 ± 0.87	-1.05 ± 0.56	-21.81 ± 0.02	10.80 ± 0.01	0.94	R
1865	0.0499	5.28	3.21	-0.02 ± 0.03	-0.25 ± 0.20	-0.25 ± 0.20	0.13 ± 0.26	-0.20 ± 0.26	-22.80 ± 0.01	11.20 ± 0.00	0.61	R
1874	0.0419	4.20	3.21	-0.12 ± 0.03	0.20 ± 0.59	0.10 ± 0.59	-1.31 ± 2.23	0.37 ± 1.68	-21.57 ± 0.02	10.71 ± 0.01	0.78	R
1880	0.0465	7.92	3.21	-0.08 ± 0.02	-0.63 ± 0.10	-0.67 ± 0.10	1.41 ± 0.18	-1.19 ± 0.14	-22.58 ± 0.01	11.11 ± 0.00	1.00	T
1890	0.0254	5.28	4.82	-0.10 ± 0.02	-0.56 ± 0.11	-0.66 ± 0.11	0.47 ± 0.15	-0.73 ± 0.12	-21.82 ± 0.02	10.81 ± 0.01	0.59	R
1968	0.0376	7.92	6.42	-0.18 ± 0.02	-0.43 ± 0.04	-0.53 ± 0.04	0.02 ± 0.08	-0.42 ± 0.08	-23.57 ± 0.01	11.51 ± 0.00	0.92	R
1977	0.0381	3.52	3.21	-0.02 ± 0.06	-0.61 ± 0.25	-0.59 ± 0.24	0.52 ± 0.44	-0.97 ± 0.26	-21.77 ± 0.01	10.79 ± 0.01	0.87	T
1988	0.0359	3.52	3.21	-0.10 ± 0.05	-0.30 ± 0.18	-0.27 ± 0.18	0.23 ± 0.35	-0.34 ± 0.16	-21.72 ± 0.01	10.77 ± 0.00	0.89	R
2003	0.0220	17.82	17.66	-0.11 ± 0.02	-0.27 ± 0.03	-0.33 ± 0.03	0.02 ± 0.09	-0.36 ± 0.09	-23.17 ± 0.01	11.35 ± 0.01	0.59	R

TABLE 5 — *Continued*

KID ^a	redshift	$r_{eff,r}$ ^b	$r_{eff,K}$ ^c	∇_{g-r} ^d	∇_{r-K} ^e	∇_{g-K} ^f	∇_t ^g	∇_Z ^h	M_K ⁱ	M_* ^j	B/T ^k	Type ^l
2027	0.0430	11.88	8.03	-0.04 ± 0.01	-0.38 ± 0.05	-0.43 ± 0.05	0.10 ± 0.08	-0.41 ± 0.10	-23.78 ± 0.01	11.59 ± 0.00	0.77	R
2040	0.0418	5.28	3.21	-0.05 ± 0.03	-0.56 ± 0.18	-0.69 ± 0.18	0.03 ± 0.23	-0.62 ± 0.26	-22.44 ± 0.01	11.06 ± 0.00	0.50	R
2064	0.0407	2.95	3.21	-0.13 ± 0.07	-0.61 ± 0.41	-0.72 ± 0.42	0.15 ± 1.41	-0.38 ± 0.88	-21.97 ± 0.01	10.87 ± 0.01	0.86	R
2068	0.0418	11.88	8.03	-0.05 ± 0.02	-0.16 ± 0.09	-0.22 ± 0.09	-0.08 ± 0.16	-0.08 ± 0.17	-23.35 ± 0.01	11.42 ± 0.00	0.57	T
2069	0.0432	5.28	4.82	-0.03 ± 0.05	-0.10 ± 0.28	-0.10 ± 0.27	0.14 ± 0.43	-0.33 ± 0.36	-21.83 ± 0.02	10.81 ± 0.01	0.52	R
2070	0.0419	3.52	3.21	-0.10 ± 0.04	-0.44 ± 0.16	-0.46 ± 0.16	0.19 ± 0.33	-0.33 ± 0.25	-21.98 ± 0.02	10.87 ± 0.01	0.70	R
2099	0.0249	13.86	6.42	-0.14 ± 0.03	-0.48 ± 0.07	-0.61 ± 0.07	0.22 ± 0.32	-0.40 ± 0.11	-21.97 ± 0.01	10.87 ± 0.00	0.62	R
2102	0.0254	5.28	4.82	-0.05 ± 0.07	-0.30 ± 0.16	-0.36 ± 0.16	0.13 ± 0.40	-0.23 ± 0.19	-21.82 ± 0.01	10.81 ± 0.00	0.58	R
2116	0.0416	11.88	6.02	-0.10 ± 0.03	-1.15 ± 0.20	-1.29 ± 0.19	0.98 ± 0.21	-1.46 ± 0.20	-23.31 ± 0.01	11.40 ± 0.00	0.51	D
2136	0.0371	7.92	6.42	-0.11 ± 0.03	-0.47 ± 0.15	-0.64 ± 0.15	-0.24 ± 0.65	-0.36 ± 0.34	-21.82 ± 0.02	10.81 ± 0.01	0.71	R
2146	0.0378	26.73	9.63	-0.06 ± 0.01	-0.33 ± 0.04	-0.38 ± 0.04	0.27 ± 0.14	-0.41 ± 0.06	-23.59 ± 0.01	11.52 ± 0.00	0.68	R
2165	0.0317	5.28	4.82	0.11 ± 0.03	0.06 ± 0.18	0.40 ± 0.18	0.31 ± 0.29	-0.25 ± 0.10	-22.29 ± 0.02	11.00 ± 0.01	0.90	R
2176	0.0470	4.50	3.21	-0.10 ± 0.04	-0.61 ± 0.54	-0.18 ± 0.51	3.19 ± 2.47	-1.68 ± 1.46	-21.79 ± 0.02	10.80 ± 0.01	1.00	R
2196	0.0391	11.88	8.03	-0.07 ± 0.03	-0.58 ± 0.14	-0.70 ± 0.14	0.20 ± 0.23	-0.48 ± 0.25	-23.35 ± 0.02	11.42 ± 0.01	0.56	R
2201	0.0496	5.28	4.82	-0.05 ± 0.04	-0.17 ± 0.22	-0.19 ± 0.22	0.33 ± 0.56	-0.21 ± 0.42	-22.42 ± 0.03	11.05 ± 0.01	0.71	R
2298	0.0336	5.28	3.21	-0.09 ± 0.03	-0.32 ± 0.19	-0.26 ± 0.20	0.40 ± 0.26	-0.54 ± 0.21	-21.86 ± 0.02	10.82 ± 0.01	0.74	R
2331	0.0418	7.92	4.82	-0.05 ± 0.04	-0.31 ± 0.14	-0.37 ± 0.15	0.28 ± 0.46	-0.39 ± 0.28	-23.00 ± 0.01	11.28 ± 0.01	0.63	R
2345	0.0458	4.14	3.21	-0.07 ± 0.03	0.10 ± 0.58	0.07 ± 0.57	-0.49 ± 1.69	0.20 ± 1.03	-22.03 ± 0.02	10.89 ± 0.01	1.00	R
2346	0.0422	3.52	3.21	-0.05 ± 0.04	-0.35 ± 0.15	-0.36 ± 0.16	0.31 ± 0.38	-0.53 ± 0.27	-22.15 ± 0.02	10.94 ± 0.01	0.92	R
2361	0.0423	2.85	3.21	0.12 ± 0.08	-0.82 ± 0.34	-0.80 ± 0.36	0.84 ± 0.47	-1.86 ± 1.04	-21.57 ± 0.02	10.71 ± 0.01	0.84	R
2362	0.0283	5.28	3.21	-0.08 ± 0.02	-0.46 ± 0.11	-0.54 ± 0.11	0.31 ± 0.17	-0.50 ± 0.13	-21.69 ± 0.01	10.76 ± 0.01	1.00	R
2366	0.0380	3.52	3.21	-0.04 ± 0.05	-0.54 ± 0.24	-0.50 ± 0.23	0.94 ± 0.55	-0.89 ± 0.45	-21.83 ± 0.01	10.81 ± 0.00	0.51	R
2368	0.0294	5.28	4.82	-0.11 ± 0.04	-0.10 ± 0.10	-0.17 ± 0.10	-0.25 ± 0.21	0.31 ± 0.14	-21.68 ± 0.01	10.75 ± 0.00	0.52	R
2371	0.0135	17.82	12.44	-0.18 ± 0.01	-0.67 ± 0.03	-0.92 ± 0.03	0.23 ± 0.09	-0.76 ± 0.05	-22.19 ± 0.01	10.95 ± 0.00	0.75	D
2377	0.0391	4.06	3.21	-0.15 ± 0.04	-0.50 ± 0.28	-0.24 ± 0.29	-0.00 ± 0.00	-0.16 ± 0.33	-21.79 ± 0.02	10.79 ± 0.01	0.90	R
2381	0.0374	5.94	3.21	-0.28 ± 0.05	-0.94 ± 0.30	-1.23 ± 0.30	-0.23 ± 0.53	-0.72 ± 0.39	-21.97 ± 0.02	10.87 ± 0.01	0.93	T
2389	0.0407	3.52	3.21	0.05 ± 0.05	-0.05 ± 0.20	-0.02 ± 0.22	0.18 ± 0.34	-0.22 ± 0.30	-21.62 ± 0.02	10.73 ± 0.01	0.73	R
2422	0.0439	4.17	3.21	-0.03 ± 0.04	-0.37 ± 0.66	-0.18 ± 0.67	0.00 ± 0.00	-0.28 ± 0.85	-21.57 ± 0.03	10.71 ± 0.01	0.61	R
2424	0.0488	5.28	4.82	-0.06 ± 0.04	-0.44 ± 0.17	-0.44 ± 0.17	0.57 ± 0.34	-0.61 ± 0.29	-22.70 ± 0.02	11.16 ± 0.01	0.51	R
2431	0.0419	3.52	3.21	-0.06 ± 0.02	-0.45 ± 0.15	-0.49 ± 0.15	0.18 ± 0.21	-0.65 ± 0.21	-22.70 ± 0.01	11.16 ± 0.00	0.95	R
2438	0.0440	7.92	4.82	-0.04 ± 0.02	-0.46 ± 0.21	-0.45 ± 0.21	0.52 ± 0.26	-0.72 ± 0.31	-22.70 ± 0.02	11.16 ± 0.01	0.68	R
2440	0.0437	4.24	3.21	0.02 ± 0.05	0.21 ± 0.38	0.16 ± 0.38	-0.22 ± 1.20	0.47 ± 0.71	-22.23 ± 0.03	10.97 ± 0.01	0.82	R
2454	0.0442	5.28	4.41	-0.03 ± 0.04	-0.96 ± 0.36	-1.25 ± 0.35	-0.26 ± 0.57	-0.67 ± 0.54	-22.35 ± 0.02	11.02 ± 0.01	0.54	D
2467	0.0452	4.06	3.21	0.04 ± 0.05	-0.63 ± 0.27	-0.47 ± 0.26	-0.00 ± 0.00	-0.39 ± 0.21	-21.71 ± 0.01	10.76 ± 0.00	0.57	R
2494	0.0402	5.28	3.21	-0.06 ± 0.03	-0.16 ± 0.12	-0.21 ± 0.12	-0.15 ± 0.33	-0.17 ± 0.15	-23.01 ± 0.01	11.28 ± 0.00	0.71	R
2495	0.0242	7.92	6.42	-0.02 ± 0.02	-0.19 ± 0.04	-0.20 ± 0.05	0.15 ± 0.13	-0.39 ± 0.10	-23.04 ± 0.01	11.30 ± 0.00	0.84	T
2528	0.0443	5.28	4.82	0.06 ± 0.03	-0.86 ± 0.13	-0.85 ± 0.13	0.19 ± 0.10	-0.79 ± 0.09	-22.62 ± 0.02	11.13 ± 0.01	0.81	R
2548	0.0281	11.88	6.42	-0.04 ± 0.01	-0.43 ± 0.04	-0.48 ± 0.04	0.41 ± 0.06	-0.83 ± 0.07	-23.13 ± 0.01	11.33 ± 0.00	0.85	T
2585	0.0437	2.15	1.61	-0.04 ± 0.07	-0.32 ± 0.50	-0.25 ± 0.49	0.91 ± 0.58	-1.10 ± 0.54	-21.65 ± 0.02	10.74 ± 0.01	0.61	R
2587	0.0437	6.60	4.82	-0.03 ± 0.03	-0.78 ± 0.27	-0.91 ± 0.52	0.45 ± 0.53	-1.28 ± 0.63	-22.44 ± 0.02	11.06 ± 0.01	0.75	R
2648	0.0466	5.28	3.21	-0.04 ± 0.02	-0.59 ± 0.14	-0.57 ± 0.14	0.41 ± 0.18	-0.74 ± 0.14	-22.76 ± 0.02	11.18 ± 0.01	0.74	R
2664	0.0415	11.88	6.42	-0.06 ± 0.02	-0.23 ± 0.15	-0.29 ± 0.15	0.01 ± 0.43	-0.33 ± 0.23	-22.78 ± 0.02	11.19 ± 0.01	0.67	T
2676	0.0313	5.28	4.82	-0.10 ± 0.03	-0.35 ± 0.10	-0.40 ± 0.10	0.09 ± 0.19	-0.40 ± 0.18	-21.92 ± 0.01	10.85 ± 0.00	0.54	R
2684	0.0308	5.28	3.21	-0.12 ± 0.05	-0.41 ± 0.12	-0.49 ± 0.12	0.02 ± 0.28	-0.38 ± 0.22	-21.68 ± 0.01	10.75 ± 0.00	0.93	R
2696	0.0400	5.28	3.21	-0.03 ± 0.03	-0.50 ± 0.28	-0.53 ± 0.28	0.24 ± 0.27	-0.62 ± 0.36	-22.28 ± 0.01	10.99 ± 0.01	0.71	R
2712	0.0421	11.88	9.63	-0.08 ± 0.02	-0.20 ± 0.05	-0.30 ± 0.05	-0.13 ± 0.12	-0.07 ± 0.10	-23.57 ± 0.01	11.51 ± 0.00	0.50	T
2756	0.0398	3.52	3.21	-0.16 ± 0.08	-0.07 ± 0.17	-0.10 ± 0.16	-0.05 ± 0.56	-0.01 ± 0.32	-22.39 ± 0.01	11.04 ± 0.00	0.59	R
2760	0.0371	5.28	3.21	-0.02 ± 0.04	-0.63 ± 0.12	-0.63 ± 0.13	1.15 ± 0.28	-1.04 ± 0.26	-22.51 ± 0.01	11.08 ± 0.00	0.70	R
2783	0.0430	7.92	4.82	-0.07 ± 0.03	-0.17 ± 0.14	-0.18 ± 0.14	0.11 ± 0.22	-0.30 ± 0.20	-23.27 ± 0.01	11.39 ± 0.00	0.72	R
2820	0.0270	7.92	4.82	-0.12 ± 0.04	-0.39 ± 0.07	-0.47 ± 0.08	0.02 ± 0.35	-0.38 ± 0.16	-22.34 ± 0.01	11.02 ± 0.00	0.83	T
2829	0.0231	7.92	3.21	-0.10 ± 0.06	-0.43 ± 0.14	-0.60 ± 0.14	-0.13 ± 0.58	-0.23 ± 0.32	-21.67 ± 0.01	10.75 ± 0.00	0.88	R
2836	0.0341	3.52	3.21	-0.04 ± 0.03	-0.14 ± 0.20	-0.14 ± 0.20	0.09 ± 0.24	-0.22 ± 0.25	-21.73 ± 0.01	10.77 ± 0.00	0.70	R
2838	0.0458	5.28	3.21	-0.03 ± 0.03	-0.29 ± 0.16	-0.29 ± 0.17	0.59 ± 0.35	-0.56 ± 0.26	-22.53 ± 0.02	11.09 ± 0.01	0.63	T
2877	0.0386	3.52	3.21	-0.02 ± 0.08	-0.28 ± 0.21	-0.24 ± 0.21	0.83 ± 0.89	-0.48 ± 0.54	-21.46 ± 0.02	10.66 ± 0.01	0.56	R
2931	0.0180	17.82	9.63	-0.03 ± 0.01	-0.29 ± 0.07	-0.31 ± 0.07	0.39 ± 0.19	-0.43 ± 0.14	-21.65 ± 0.02	10.74 ± 0.01	0.56	R
2971	0.0360	5.28	3.21	-0.05 ± 0.05	-0.29 ± 0.16	-0.26 ± 0.17	0.97 ± 0.61	-0.52 ± 0.32	-22.07 ± 0.01	10.91 ± 0.00	1.00	R
2982	0.0425	7.92	4.82	-0.08 ± 0.02	-0.42 ± 0.11	-0.53 ± 0.11	0.02 ± 0.14	-0.41 ± 0.14	-23.27 ± 0.01	11.39 ± 0.00	0.71	R

TABLE 5 — *Continued*

42

KID ^a	redshift	$r_{eff,r}$ ^b	$r_{eff,K}$ ^c	∇_{g-r} ^d	∇_{r-K} ^e	∇_{g-K} ^f	∇_t ^g	∇_Z ^h	M_K ⁱ	M_* ^j	B/T ^k	Type ^l
2983	0.0446	5.28	3.21	-0.16 ± 0.05	-0.27 ± 0.17	-0.34 ± 0.17	-0.00 ± 0.00	-0.16 ± 0.31	-22.49 ± 0.02	11.07 ± 0.01	0.90	R
3049	0.0449	4.17	3.21	-0.05 ± 0.05	-0.48 ± 0.52	-0.36 ± 0.53	0.01 ± 0.00	-0.42 ± 0.50	-21.42 ± 0.03	10.65 ± 0.01	0.62	R
3073	0.0229	11.88	6.42	-0.03 ± 0.02	-0.35 ± 0.03	-0.40 ± 0.04	0.10 ± 0.11	-0.48 ± 0.09	-22.36 ± 0.01	11.03 ± 0.00	0.54	R
3097	0.0438	3.52	3.21	0.03 ± 0.07	0.02 ± 0.36	0.07 ± 0.40	0.17 ± 0.73	-0.03 ± 0.68	-21.44 ± 0.02	10.66 ± 0.01	0.50	R
3122	0.0487	3.22	3.21	-0.32 ± 0.07	0.23 ± 0.29	0.46 ± 0.29	0.19 ± 0.97	0.26 ± 0.58	-21.48 ± 0.02	10.67 ± 0.01	0.52	R
3124	0.0415	7.92	8.03	-0.03 ± 0.01	-0.01 ± 0.05	-0.02 ± 0.05	0.00 ± 0.00	0.04 ± 0.09	-23.24 ± 0.02	11.38 ± 0.01	0.56	T
3131	0.0437	7.92	4.82	-0.04 ± 0.02	-0.32 ± 0.17	-0.31 ± 0.17	0.59 ± 0.38	-0.44 ± 0.28	-22.52 ± 0.02	11.09 ± 0.01	0.50	R
3148	0.0291	11.88	8.03	-0.06 ± 0.01	-0.08 ± 0.07	-0.12 ± 0.07	-0.05 ± 0.15	-0.05 ± 0.11	-22.09 ± 0.02	10.91 ± 0.01	0.59	R
3191	0.0442	5.28	4.82	-0.05 ± 0.05	-0.02 ± 0.46	-0.00 ± 0.53	0.30 ± 0.58	0.43 ± 0.54	-21.99 ± 0.03	10.88 ± 0.01	0.64	T
3218	0.0431	17.82	11.24	-0.06 ± 0.01	-0.31 ± 0.11	-0.33 ± 0.11	0.12 ± 0.16	-0.41 ± 0.17	-23.17 ± 0.03	11.35 ± 0.01	0.69	R
3247	0.0450	5.28	3.21	-0.05 ± 0.04	-0.53 ± 0.15	-0.54 ± 0.17	0.57 ± 0.37	-0.99 ± 0.22	-22.35 ± 0.01	11.02 ± 0.01	1.00	R
3308	0.0345	3.52	3.21	-0.13 ± 0.07	-0.39 ± 0.64	-0.37 ± 0.63	0.24 ± 0.72	-0.46 ± 0.46	-21.36 ± 0.01	10.62 ± 0.01	0.87	T
3343	0.0456	5.28	3.21	-0.06 ± 0.04	-0.30 ± 0.18	-0.30 ± 0.19	0.94 ± 0.74	-0.64 ± 0.36	-22.37 ± 0.03	11.03 ± 0.01	0.62	R
3374	0.0268	11.88	4.82	-0.10 ± 0.02	-0.63 ± 0.08	-0.77 ± 0.09	0.17 ± 0.15	-0.69 ± 0.13	-21.82 ± 0.01	10.81 ± 0.00	0.57	T
3392	0.0388	11.88	6.42	-0.03 ± 0.01	-0.22 ± 0.07	-0.25 ± 0.07	0.14 ± 0.17	-0.20 ± 0.12	-22.90 ± 0.02	11.24 ± 0.01	0.61	R
3402	0.0437	4.00	3.21	-0.06 ± 0.03	-0.26 ± 0.15	-0.29 ± 0.15	0.18 ± 0.22	-0.57 ± 0.16	-22.38 ± 0.01	11.03 ± 0.01	0.91	R
3418	0.0448	17.82	12.84	-0.07 ± 0.01	-0.22 ± 0.06	-0.26 ± 0.05	0.01 ± 0.09	-0.23 ± 0.11	-24.15 ± 0.01	11.74 ± 0.00	0.99	T
3438	0.0250	3.52	3.21	-0.04 ± 0.03	-0.69 ± 0.15	-0.72 ± 0.15	0.66 ± 0.21	-0.94 ± 0.13	-21.46 ± 0.01	10.66 ± 0.00	0.91	R
3440	0.0293	11.88	8.03	-0.07 ± 0.01	-0.24 ± 0.04	-0.28 ± 0.04	0.11 ± 0.11	-0.29 ± 0.07	-23.35 ± 0.01	11.42 ± 0.00	0.66	R
3442	0.0182	7.92	6.42	-0.07 ± 0.02	-0.32 ± 0.06	-0.35 ± 0.06	0.11 ± 0.12	-0.52 ± 0.10	-21.88 ± 0.01	10.83 ± 0.00	0.56	R
3457	0.0493	3.10	3.21	0.02 ± 0.12	-0.33 ± 0.23	0.72 ± 0.70	-0.54 ± 2.72	0.87 ± 2.03	-21.43 ± 0.02	10.65 ± 0.01	0.68	R
3468	0.0188	7.92	6.42	-0.04 ± 0.04	-0.14 ± 0.06	-0.19 ± 0.06	-0.00 ± 0.00	-0.16 ± 0.08	-22.24 ± 0.01	10.98 ± 0.00	0.80	R
3471	0.0176	11.88	4.82	-0.03 ± 0.01	-0.38 ± 0.04	-0.39 ± 0.04	0.33 ± 0.08	-0.54 ± 0.06	-22.54 ± 0.00	11.09 ± 0.00	0.75	T
3499	0.0283	11.88	6.42	-0.07 ± 0.02	-0.35 ± 0.10	-0.45 ± 0.10	-0.07 ± 0.16	-0.31 ± 0.12	-22.42 ± 0.01	11.05 ± 0.01	0.75	R
3523	0.0498	2.35	3.21	-0.14 ± 0.07	-0.28 ± 0.16	-0.29 ± 0.17	0.61 ± 0.63	-0.38 ± 0.29	-22.39 ± 0.01	11.04 ± 0.00	0.64	R
3551	0.0478	5.35	3.21	-0.00 ± 0.03	-1.74 ± 0.77	-1.44 ± 0.77	1.96 ± 1.98	-2.27 ± 1.29	-21.69 ± 0.03	10.76 ± 0.01	0.59	R
3582	0.0182	7.92	4.82	-0.04 ± 0.01	-0.51 ± 0.05	-0.54 ± 0.05	0.24 ± 0.11	-0.68 ± 0.06	-21.42 ± 0.01	10.65 ± 0.00	0.87	R
3620	0.0431	7.92	4.82	-0.08 ± 0.02	-0.25 ± 0.17	-0.28 ± 0.17	0.39 ± 0.27	-0.40 ± 0.20	-22.76 ± 0.02	11.19 ± 0.01	0.70	R
3644	0.0445	5.28	3.21	0.00 ± 0.04	-0.06 ± 0.45	0.31 ± 0.43	1.11 ± 0.70	-0.69 ± 0.46	-21.79 ± 0.02	10.80 ± 0.01	1.00	R
3657	0.0280	17.82	7.62	-0.13 ± 0.02	-0.81 ± 0.08	-0.91 ± 0.07	0.14 ± 0.08	-1.64 ± 0.06	-23.28 ± 0.01	11.39 ± 0.00	0.85	D
3676	0.0365	3.52	3.21	-0.06 ± 0.04	-0.23 ± 0.15	-0.29 ± 0.16	0.03 ± 0.35	-0.34 ± 0.31	-22.01 ± 0.01	10.88 ± 0.00	0.94	R
3689	0.0419	7.92	6.42	-0.07 ± 0.02	-0.26 ± 0.09	-0.32 ± 0.09	0.00 ± 0.08	-0.36 ± 0.10	-23.77 ± 0.01	11.59 ± 0.00	0.85	T
3710	0.0179	7.92	6.42	-0.03 ± 0.01	-0.05 ± 0.03	-0.08 ± 0.03	-0.03 ± 0.10	-0.06 ± 0.07	-22.33 ± 0.00	11.01 ± 0.00	0.96	R
3725	0.0499	11.88	8.03	-0.04 ± 0.02	-0.30 ± 0.08	-0.36 ± 0.08	0.27 ± 0.35	-0.25 ± 0.17	-23.12 ± 0.02	11.33 ± 0.01	0.59	R
3726	0.0494	5.10	3.21	-0.11 ± 0.04	-1.16 ± 0.25	-1.33 ± 0.25	0.83 ± 0.30	-1.53 ± 0.34	-22.48 ± 0.01	11.07 ± 0.00	0.62	R

Kim & Im

^a Object ID from the catalog of Kaviraj (2010)^b Effective radius in r -band (arcsec)^c Effective radius in K -band (arcsec)^d Color gradient in $g-r$ ^e Color gradient in $r-K$ ^f Color gradient in $g-K$ ^g Age gradient^h Metallicity gradientⁱ Absolute K -band magnitude (AB)^j Stellar mass from absolute K -band magnitude^k Bulge to total light ratio^l Morphological type (R:relaxed, T:tidal-feature, D:dust-feature)